

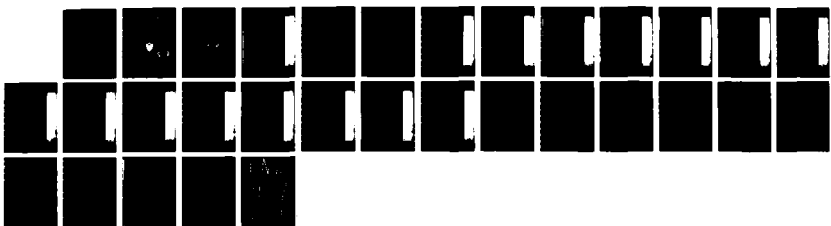
RD-A105 133

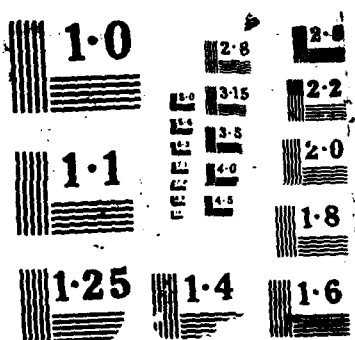
FINAL REPORT ON CONTRACT F49628-85-C-0026 VOLUME 5(U)
PRINCETON UNIV NJ DEPT OF MECHANICAL AND AEROSPACE
ENGINEERING 5 A ORSZAG MAY 87 AFOSR-TR-87-1349-VOL-5
UNCLASSIFIED FF9628-85-C-0026

1/1

F/G 20/4

NL





AD-A185 133

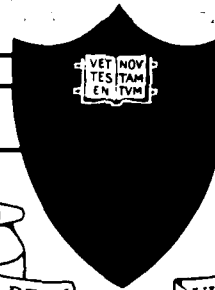
AFOSR-TX-87-1849

2
DTIC FILE COPY

FINAL REPORT ON
AFOSR CONTRACT F49620-85-C-0026

Steven A. Orszag, Principal Investigator
Department of Mechanical and Aerospace Engineering
Princeton University
Princeton, NJ 08544

Volume 5



DTIC
SELECTED
SEP 30 1987
S D
C E D

DISTRIBUTION STATEMENT A

Approved for public release
Distribution Unlimited

PRINCETON UNIVERSITY

87 9 24 248

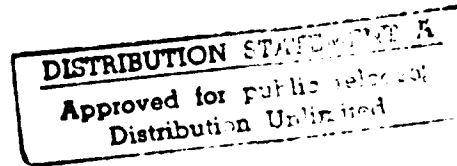
2

**FINAL REPORT ON
AFOSR CONTRACT F49620-85-C-0026**

Steven A. Orszag, Principal Investigator
Department of Mechanical and Aerospace Engineering
Princeton University
Princeton, NJ 08544

Volume 5

DTIC
ELECTE
SEP 30 1987
S D
C D



Secondary Instability of Free Shear Flows

Marco E. Brachet¹, Ralph W. McIrvine²,
Steven A. Orzag³, James J. Riley⁴

Abstract

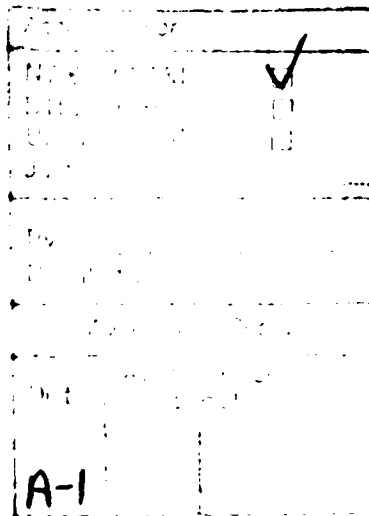
The three-dimensional stability of saturated two-dimensional vertical states of planar mixing layers and jets is studied by direct integration of the Navier-Stokes equations. Small-scale instabilities are shown to exist for spanwise scales at which classical linear modes are stable. These modes grow on convective time scales, extract their energy from the mean flow, and persist to moderately low Reynolds numbers. Their growth rates are comparable to the most rapidly growing inviscid instability and to the growth rates of two-dimensional subharmonic (pairing) modes. The three-dimensional modes do not appear to saturate in quasi-steady states. Indeed, they seem to lead directly to chaotic results as presented for the resulting three-dimensional turbulent states.

¹ CNRS, Observatoire de Nice, 06-Nice, France

² Flow Research, Inc., Kent, WA 98032

³ Princeton University, Princeton, NJ 08544

⁴ University of Washington, Seattle, WA 98105



REPORT DOCUMENTATION PAGE

1a. REPORT SECURITY CLASSIFICATION Unclassified	1b. RESTRICTIVE MARKINGS										
2a. SECURITY CLASSIFICATION AUTHORITY	3. DISTRIBUTION/AVAILABILITY OF REPORT Approved for Public Release; distribution is unlimited										
2b. DECLASSIFICATION/DOWNGRADING SCHEDULE											
4. PERFORMING ORGANIZATION REPORT NUMBER(S)	5. MONITORING ORGANIZATION REPORT NUMBER(S) AFOSR-TR- 87-1340										
6a. NAME OF PERFORMING ORGANIZATION Princeton University	6b. OFFICE SYMBOL (If applicable)	7a. NAME OF MONITORING ORGANIZATION AFOSR/NA									
7c. ADDRESS (City, State and ZIP Code) Princeton University/ Princeton, NJ 08544	7b. ADDRESS (City, State and ZIP Code) Building 410 Bolling AFB DC 20332-6448										
8a. NAME OF FUNDING/SPONSORING ORGANIZATION AFOSR/NA	8b. OFFICE SYMBOL (If applicable)	9. PROCUREMENT INSTRUMENT IDENTIFICATION NUMBER F49620-85-C-0026									
10c. ADDRESS (City, State and ZIP Code) Bolling Air Force Base Washington, DC 20332-6448	10. SOURCE OF FUNDING NOS. <table border="1"><tr><th>PROGRAM ELEMENT NO.</th><th>PROJECT NO.</th><th>TASK NO.</th><th>WORK UNIT NO.</th></tr><tr><td>61102F</td><td>2307</td><td>A2</td><td></td></tr></table>			PROGRAM ELEMENT NO.	PROJECT NO.	TASK NO.	WORK UNIT NO.	61102F	2307	A2	
PROGRAM ELEMENT NO.	PROJECT NO.	TASK NO.	WORK UNIT NO.								
61102F	2307	A2									
11. TITLE (Include Security Classification) Final Report on Contract F49620-85-C-0026 Vol. 5	12. DATE OF REPORT : Yr., Mo., Day May, 1987										
13. PAGE COUNT 15											

14. SUPPLEMENTARY NOTATION			
----------------------------	--	--	--

15. COSATI CODES		16. SUBJECT TERMS (Continue on reverse if necessary and identify by block numbers)	
FIELD	GROUP	SUB. GR	
		Turbulence, Numerical Simulation	

ABSTRACT (Continue on reverse if necessary and identify by block numbers)

This report consists of papers that summarize work done on this research project. The major results include: 1) The development and application of the renormalization group method to the calculation of fundamental constants of turbulence, the construction of turbulence transport models, and large-eddy simulations; 2) The application of RNG methods to turbulent heat transfer through the entire range of experimentally accessible Reynolds numbers; 3) The discovery that high Reynolds number turbulent flows tend to act as if they had weak nonlinearities, at least when viewed in terms of suitable 'quasi-particles'; 4) The further analysis of secondary instability mechanisms in free shear flows, including the role of these instabilities in chaotic, 3-D free shear flows; 5) The further development of numerical simulations of turbulent spots in wall bounded shear flows; 6) The study of cellular automata for the solution of fluid mechanical problems; 7) The clarification of the relationship between the hyperscale instability of anisotropic small-scale flow structures to long-wavelength perturbations and the cellular automaton description

DISTRIBUTION/AVAILABILITY OF ABSTRACT <input checked="" type="checkbox"/> CLASSIFIED/UNLIMITED <input checked="" type="checkbox"/> SAME AS RPT <input checked="" type="checkbox"/> OTS USERS	21. ABSTRACT SECURITY CLASSIFICATION Unclassified
NAME OF RESPONSIBLE INDIVIDUAL Dr James M McMichael	22a. TELEPHONE NUMBER (Include Area Code) (202) 767-4936
	22c. OFFICE SYMBOL AFOSR/NA

STRACT, continued from other side

fluids; 8) The development of efficient methods to analyze the structure of strange attractors in the description of dynamical systems; 9) The analysis of multiscale instability as a mechanism for destabilization of coherent flow structures.

1 Introduction

Free shear flows like those of mixing layers and jets differ from wall bounded flows in the sense that they are typically unidirectional and, hence, are subject to inviscid instabilities. Thus, it may be thought that the process of transition to turbulence in free-shear flows would be inherently simple and amenable to analysis. Indeed, observations by Winant & Browand (1974), Brown & Roshko (1974), Wygnanski et al (1979), Ho & Huang (1982), Hussain (1984), and others show the central role played by two-dimensional dynamical processes through transitional regimes in these flows. While three-dimensional small scales are observed (Miles 1972, Rennel et al 1979), they may not destroy the large-scale two-dimensional structure (Browand & Trout 1980). In contrast, studies of wall-bounded flows have emphasized the central role of three-dimensional effects in their breakdown to turbulence.

In this paper, we investigate the nature of linear instabilities of saturated nonlinear two-dimensional flow states that arise from the primary inviscid instability of free shear flows. It is shown that these saturated two-dimensional states are subject to a class of strongly unstable three-dimensional modes that are present even at moderately low Reynolds numbers. It is possible that these three-dimensional instabilities can explain some of the initial stages of three-dimensional transition in free shear flows. We find that the two- or three-dimensional character of these free shear flows depend crucially on inlet conditions as there is a close competition between the various modes of instability to be discussed below.

The approach followed here is similar to that used by Orszag & Patera (1980, 1981, 1983) in studies of secondary instabilities in wall-bounded flows. The parallel laminar flow is perturbed initially by a finite amplitude two-dimensional disturbance that is allowed to evolve and to saturate in a quasi-steady state. The stability of this finite amplitude vortical state to both subharmonic (pairing) two-dimensional

modes and smaller-scale three-dimensional modes is then studied by numerical solution of the full three-dimensional time-dependent Navier-Stokes equations. The character of the pairing instability was first explained theoretically by Kelly (1967) and numerically by Rainak, Sherman & Corcos (1974) and Collins (1982) for strained flows and by Hiley & Metcalfe (1990) and Pierrehumbert & Womall (1982), for unstrained flows; the present results confirm the strength of this kind of mode.

Pierrehumbert & Womall (1982) have made a study of the linear two- and three-dimensional instabilities of a spatially periodic inviscid shear layer that is closely related to the present study. They consider the stability characteristics of the modulational instability of two-dimensional wavy-modulated mixing layers with velocity fields

$$u = \rho \sin r / (\cosh r - \rho \cos x) \quad (1.1)$$

$$w = \rho \sin r / (\cosh r - \rho \cos x)$$

(Stuart 1967) for $0 < \rho < 1$, and study subharmonic pairing instabilities and a new 'translative' three-dimensional instability. In contrast, we consider here both the linear and nonlinear stability characteristics of time-developing viscous shear layers. The three-dimensional secondary instability studied here is both the analog of the translative instability and the generalization of the instability analyzed by Orszag & Patera for wall-bounded flows.

* Note that for $\rho < 1$, the basic flow state (1.1) is of the form $\tanh r / r + \phi \tanh^2(r)$. This flow state is an inviscid neutrally stable perturbation of the mixing layer $\tanh r / r$. At wavenumber 1, there are no primary two-dimensional instabilities that can compete with the subharmonic and secondary instabilities. In contrast, the results to be reported in Section 3 involve unstable primary perturbations to the mixing layer.

The Navier-Stokes equations are solved in the form

$$\frac{d\hat{v}}{dt} = \hat{v} \cdot \hat{u} - \tau_h + v \cdot \hat{v}^2 \hat{v} \quad (2.1)$$

$$\hat{v} \cdot \hat{v} = 0$$

where $\hat{u} = v \times \hat{v}$ is the vorticity and $\tau_h = p + 1/2 v^2$ is the pressure head.

Periodic boundary conditions are applied in the streamwise, x , and spanwise y directions.

$$\hat{v}(x + \frac{a}{2}, y, z, t) = \hat{v}(x, y, z, t) \quad (2.3)$$

$$\hat{v}(x, y + 2\pi/a, z, t) = \hat{v}(x, y, z, t)$$

while the flow is assumed quiescent ($\hat{v} = U_1 \hat{z}$, U_1 constants) as $t \rightarrow -\infty$. Note that the assumed periodicity length is $4\pi/a$ to accommodate both the primary mode with x -wavenumber a and its subharmonic with x -wavenumber $1/a$.

Pierrehumbert & Widnall (1982) point out that Floquet theory implies that the Navier-Stokes equations linearized about a time-periodic \hat{u} admit solutions of the more general form $\hat{v}(x, y, z, t) = \phi(t) \hat{v}(x, y, z)$ where ϕ is periodic in x with the same periodicity as the basic flow and \hat{v} is arbitrary. However, Pierrehumbert & Widnall consider only the subharmonic and primary cases. The analysis, which has not yet been done for more general ϕ , may yield important new results. Busse (1979) points out the importance of these general ϕ modes in Rayleigh convection. The present study is restricted to ϕ being a half-integer multiple of the primary wavenumber because our code is fully nonlinear with the periodicity condition (2.3).

The assumption of periodicity in the streamwise x direction is unrealistic in a spatially growing mixing layer unless the modes being studied are localized in x and grow much more rapidly than the shear layer spreads. These latter approximations seem reasonably well justified for the three-dimensional modes studied here (see Sec. 3). However, future work using inflow-outflow boundary conditions in x should clarify the role of non-parallel effects in free-shear flows.

The dynamical equations are solved using pseudospectral methods in which the flow variables are expanded in the series

$$\hat{v}(x, y, z, t) = \sum_{|m| < \frac{1}{2}N} \sum_{|n| < \frac{1}{2}N} \sum_{p=0}^{p=N} \hat{u}(m, n, p, t) e^{imx} e^{inyc} e^{ipz} \quad (2.4)$$

where n and p are integers and m is a half-integer when pairing is allowed and a whole integer if pairing is excluded. Here $2 = 1/\pi$ is a transformed x -coordinate satisfying $2 = \pm 1$ when $x = \pm a$. Two choices of $\phi(z)$ have been studied.

$$2 = \tanh \frac{z}{L} \quad (|z| < a, |z| < 1) \quad (2.5)$$

and

$$2 = \frac{2}{L^2 + Lz} \quad (|z| < a, |z| < 1) \quad (2.6)$$

where L is a suitable scale factor. With these mappings, derivatives with respect to z are evaluated pseudospectrally using the relations

$$\frac{d\hat{v}}{dz} = \frac{1}{L} (1 - z^2) \frac{\partial \hat{v}}{\partial z} \quad (2.7)$$

$$\frac{\partial^2 \hat{v}}{\partial z^2} = \frac{1}{L} \sqrt{1 - z^2} \frac{\partial^2 \hat{v}}{\partial z^2} \quad (2.8)$$

for (2.5), (2.6), respectively.

Time stepping is done by a fractional step method in which the nonlinear terms are marched in time using a second-order

Adams-Basforth scheme while pressure head and viscous effects are imposed implicitly using Crank-Nicolson differencing

This scheme is globally 1 cond order accurate in time, despite time splitting (Deville & Orszag 1983). because the various split operators commute in the case of quiescent boundary conditions at $\mathbf{r} = \mathbf{0}$

There is one further technical detail regarding the numerical method that should be discussed here. Various Poisson equations like

$$\frac{d^2\eta}{dz^2} - (m^2 + n^2)\eta = g(z) \quad (|z| \leftarrow \infty) \quad (2.9)$$

are solved by expansion in the eigenfunctions of d^2/dz^2 :

$$\frac{d^2}{dz^2} e_k(z) = \lambda_k e_k(z) \quad (|z| \leftarrow \infty) \quad (2.10)$$

Thus, if

$$g(z) = \sum_{k=0}^P q_k e_k(z)$$

$$\eta(z) = \sum_{k=0}^P \frac{q_k}{\lambda_k - (m^2 + n^2)} e_k(z) \quad (2.11)$$

We remark that this technique gives spectrally accurate solutions, despite the fact that the continuous version of the eigenvalue problem (2.10) has only a continuous, and hence singular, spectrum. Also, note that all the eigenvalues λ_k are real and non-positive; for both mappings (2.5) and (2.6), there are precisely three zero eigenvalues $\lambda_1, \lambda_2, \lambda_3$. One of these zero eigenmodes, λ_1 , is physical, viz. $e_1(z) = 1$, but the other two are highly oscillatory and unphysical. Indeed, since the spectral (Chebyshev) derivative of $T_P(z)$ vanishes except at $z = \pm 1$, $e_2(z) = T_P(z)$ is a zero eigenfunction of d^2/dz^2 : $T_P'(z) = (-1)^P$ at the Chebyshev collocation points $z_i = \cos \pi i / P$. The third zero eigenmode oscillates and grows

roughly like z . When $m = n = 0$, the incompressibility constraint (2.2) requires that this mode of the z -velocity field vanish identically so there is no difficulty with the zero pressure eigenvalues $\lambda_1, \lambda_2, \lambda_3$.

Comparisons of the behavior of linear Orr-Sommerfeld eigenmodes obtained using the mappings (2.5) and (2.6) show that (2.6) gives a superior representation of these modes unless L is fine tuned, which is not convenient in the nonlinear dynamical runs. Some representative results are given in Table 1. Notice that as λ increases, the optimal choice of map scale L decreases. Also, notice that the accuracy of the eigenvalue is much more sensitive to L for the hyperbolic tangent mapping (2.5) than for (2.6).

The nonlinear time-dependent Navier-Stokes code has been tested for the generalized Taylor-Green vortex flow (2.12) and for the behavior of linearized eigenfunctions, with satisfactory agreement being achieved with power series in λ (Brechet et al 1983) and linear behavior, respectively.

There is one case in which it seems that the hyperbolic tangent mapping (2.5) is more convenient than the algebraic mapping (2.6). This flow is the generalized Taylor-Green vortex flow that develops from the initial conditions

$$\begin{aligned} u(x, y, z, 0) &= \sin \pi \cos y \cosh^2 z \\ v(x, y, z, 0) &= -\cos x \sin y \cosh^2 z \\ w(x, y, z, 0) &= 0 \end{aligned} \quad (2.12)$$

The evolution of this flow seems best studied, either by power series or initial value methods, using (2.5) with $\lambda = 1$. The time evolution of this free shear flow is remarkably similar to that of the periodic Taylor-Green vortex (Brechet et al 1983).

3. Results for Mixing Layers

In this Section, results are reported for the evolution of initial velocity fields of the form

$$\hat{v}(x, y, z, 0) = U_0(z) + \text{Re}[\lambda_0 \hat{v}_{10}(z)e^{i\omega_0 t} + \lambda_1 \hat{v}_{11}(z)e^{\frac{1}{2}i\omega_1 t}] + \lambda_{11} \hat{v}_{111}(z)e^{i(\omega_0 + \omega_1)t}] \quad (3.1)$$

Table 1. Growth Rates $\text{Im}(\zeta)$ of the Orr-Sommerfeld Eigenfunctions for the Mixing Layers $U_0(z) = \tanh z$

		B-z wavenumber σ										
		0.35			0.5			0.75				
		Number of Chebyshev Polynomials (P+1)										
		Hyperbolic Map (2.5)										
0	0.5	1.534	1.375	1.238	0.591	0.457	0.360	0.150	0.150			
1	1	0.959	0.970	0.796	0.393	0.351	0.141	0.138	0.137			
2	2	0.631	0.614	0.405	0.346	0.342	0.342	0.137	0.137			
3	3	0.412	0.598	0.597	0.324	0.347	0.342	0.041	0.136			
4	4	0.258	0.597	0.597	0.315	0.322	0.342	5	0.045			
5	5	0.202	0.576	0.594	5	0.321	5	5	0.046			

Hyperbolic Map (2.6)

		B-z wavenumber σ										
		0.35			0.5			0.75				
		Number of Chebyshev Polynomials (P+1)										
		Hyperbolic Map (2.5)										
0	0.5	0.646	0.548	0.548	0.345	0.346	0.187	0.133	0.133			
1	1	0.193	0.598	0.597	0.346	0.342	0.342	0.137	0.137			
2	2	0.600	0.587	0.597	0.342	0.342	0.342	0.136	0.137			
3	3	0.597	0.587	0.597	0.325	0.347	0.342	0.371	0.136			
4	4	0.592	0.587	0.597	0.09	0.323	0.342	5	0.041			

- here the Reynolds number is $1/\epsilon = 100$ and the eigenvalue is the critical wave speed c for a terminal mode of the form $u = u_m(z)$. For the most rapidly growing mode listed here, $Re = 0$.
- ^s indicates that all modes are stable with the indicated parameter values

The laminar mean profile is assumed to be the mixing layer profile $U_0(z) = \tanh z$ and $\Psi_0(z)$ is normalized so that $\max|\Psi_0(z)| = 1$. The initial functions $\Psi_0(z)$ are normally chosen as the most unstable eigenfunctions of the linear Orr-Sommerfeld equation with the wavenumbers given in (3.1). In this representation, λ_{10} is the amplitude of the primary two-dimensional component, $\lambda_{1/2}$ is the amplitude of its subharmonic or pairing mode, and λ_{11} is the amplitude of the primary three-dimensional wave. In all cases, the initial conditions are chosen so that $\lambda_{1/2}, \lambda_0, \lambda_{11} \ll \lambda_{10}$. Typically $\lambda_{10} = 0.25$. Also, the momentum thickness Reynolds number for the undisturbed flow is $R = 1/\epsilon$.

In the absence of subharmonic and three dimensional perturbations ($\lambda_{1/2}, \lambda_0, \lambda_{11} = 0$), the two-dimensionally perturbed flow quickly saturates to a quasi-steady state. In Figure 1, a plot is given of the time evolution of the two dimensional disturbance energy $F(t)$ for various initial amplitudes λ_{10} .

- The Reynolds numbers of the flows discussed below, while modest, are much greater than that of the onset of linear instability ($Re_{\text{crit}} = 4$), so that even the linear modes are effectively inviscid. In this case, damped modes may lie only in the continuous spectrum (Drazin & Reid 1981) and so are singular. Whenever (3.1) calls for such a singular contribution to the initial condition (3.1), we choose instead the flow component $u_{nm} = w_{10}$ of the primary mode (with u_{nm} and w_{nm} determined by incompressibility).

Here

$$\mathcal{E}_{mn}(t) = \int_{-\infty}^{\infty} dz |\hat{v}_{mn}(z, t)|^2 \quad (13.2)$$

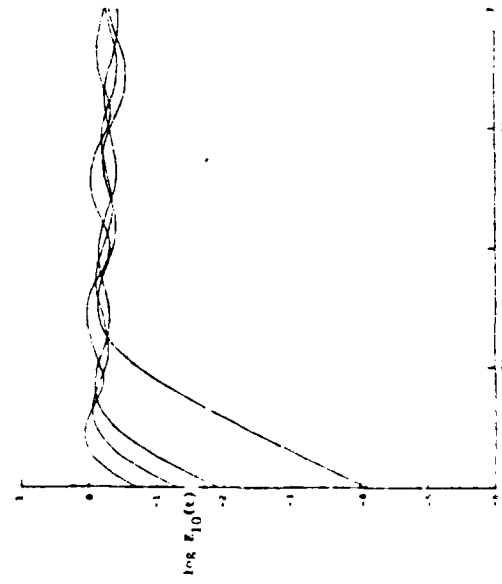
where

$$\hat{v}_{mn}(z, t) = \sum_p \hat{u}(m, n, p, t) T_p(z) \quad (13.3)$$

and u is defined by (2.4). It is apparent that E_{10} saturates into a finite-amplitude vortical state on a time scale of order 10. Indeed the mean flow $\tanh z$ is inviscidly unstable to the perturbation A_{10} with maximum growth rate roughly 0.2 when $\alpha = 0.44$. (The range of inviscidly unstable wavenumbers for the $\tanh z$ profile is $0 < \alpha < 1$. Also, note that N we used a length scale in which the wavelength of the perturbation is of order unity (rather than our unity in which the shear layer thickness is order 1), saturation of E_{10} would occur on a time scale of order 1.3 in Fig. 2. a plot is given of an instantaneous spanwise vorticity distribution in the developed two-dimensional flow.

Comparison of the energy evolution plotted in Figs. 3(a) and 3(b) shows that the initial phase of the subharmonic perturbation can affect its growth rate but not the eventual growth and saturation of the subharmonic. The present calculations differ from those of Riley & Meicelle (1980) and Painalki et al. (1978) in that the initial disturbances are chosen to be computationally infinitesimal in our runs in contrast to their finite-amplitude initial perturbations (Also Painalki et al. study stratified flows). While phase does affect the initial subharmonic growth rate, the perturbation eventually achieves its optimal growth rate during our long time runs. We conclude that the 'vortex shedding' process found by Painalki et al. is a finite amplitude effect, not reproducible in the present long-time runs.

Figure 1.
A plot of $\log E_{10}(t)$ vs t for runs with $A_{10} = A_{11} = 0$ and $A_{10} = 0.5, 0.125, 0.01$. Here the Reynolds number is $R = 400$, $U_0(z) = \tanh z$, the spectral cut-offs in (2.4) are $M = N = 1, P = 32$, resolution $\Delta z = 1 \times 32$ with no pairing modes). the wavenumber is $\alpha = 0.4$, and the time step is $\Delta t = 0.02$. Note that the flow saturates into a vortical state nearly independent of the initial perturbation. Before such saturation occurs, the perturbation grows linearly like an Orr-Sommerfeld eigenfunction



The saturated two-dimensional flow state discussed above can be unstable to subharmonic perturbations. A 1/2.0 in (13.1). for suitable α (Kelly 1987). In Figure 3. we plot the evolution of the

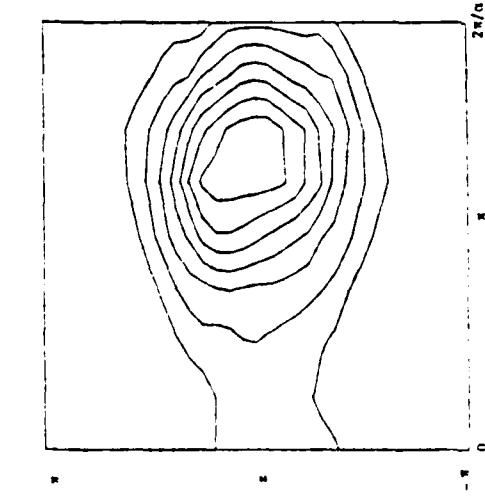


Figure 2. A contour plot of spanwise (y) vorticity contours for the saturated flow state of the mixing layer at $R = 400$. The vorticity is nearly stationary.

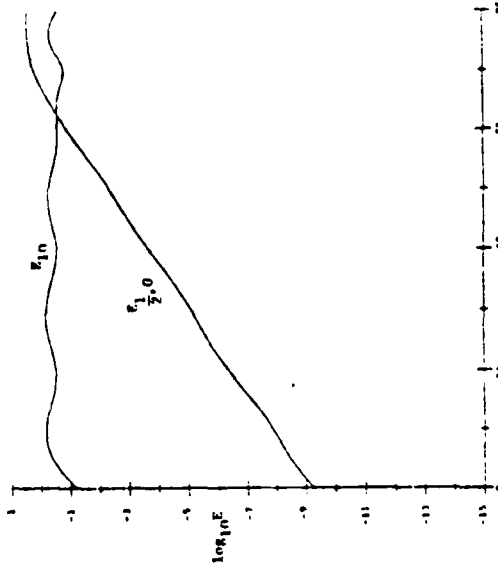


Figure 2

Plots of the evolution of $E(10t)$ and the two-dimensional pairing mode energy $E_1(0t)$ as functions of time. Here $\hbar = 400$, $U(0t) = \tanh 2$, $A_{10} = 1$, $A_{11} = 3 \times 10^{-4}$, $M = 8$, $N = 1$, $P = 32$, resolution $16 \times 1 = 32$ with pairing modes $\alpha = 0.5$ and $\beta = 0.02$. (a) and (b) differ by a 90° phase shift of initial subharmonic perturbation.

subharmonic perturbation energies $E_{1/2,0}(t)$ as well as the primary two dimensional energy $E_{10,0}(t)$. Here we choose $\alpha_{10} = 0.25$ and $\alpha_{1/2,0} = 3 \times 10^{-4}$. In Figure 3(a), the primary and subharmonic perturbation vorticity are initially in phase; in Figure 3(b) they are initially out of phase. This subharmonic instability of the saturated two dimensional vortical states is inviscid in character as its growth rate asymptotes to a finite limit as R increases. The growth rate $\alpha_{1/2,0} = 0.2$ for $\alpha = 0.8$. These growth rates are not significantly larger than the linear inviscid growth rates of Orr-Sommerfeld modes; however, pairing perturbations are significant because the nonlinear saturation of the two-dimensional Orr-Sommerfeld modes allows the pairing modes to achieve finite amplitudes at later times. The evolution of the spanwise vorticity distribution during pairing instability is revealed by the contour plots given in Fig. 4. The energetics of the pairing instability is revealing. Energetic transfers to and from the pairing mode may be decomposed as

$$\frac{1}{2} \frac{dE_{1,0}}{dt} + \frac{1}{2} \frac{dE_{1/2,0}}{dt} = \gamma_M + \gamma_{2-D} + \gamma_V \quad (13.4)$$

where γ_M involves the nonlinear interaction of the pairing mode with the mean flow, γ_{2-D} involves the nonlinear interaction of the pairing mode and all other two-dimensional modes, and γ_V the viscous dissipation of pairing energy. Here γ_M and γ_{2-D} involve sums over nonlinear terms in the Navier-Stokes equations but are unaffected by pressure; γ_V is proportional to the enstrophy in the pairing mode. In Fig. 5, a plot is given of these transfer terms as a function of time. It appears that the pairing mode extracts most of its energy from the mean flow and grows no faster than in the absence of the two-dimensional primary component. The important conclusions are that the presence of the saturated two-dimensional primary does not turn off the pairing mode and that the growth rate of this latter mode is of order that observed in the primary two-dimensional instability. These results imply that even a small pairing perturbation will quickly achieve finite amplitude after the primary mode saturates.

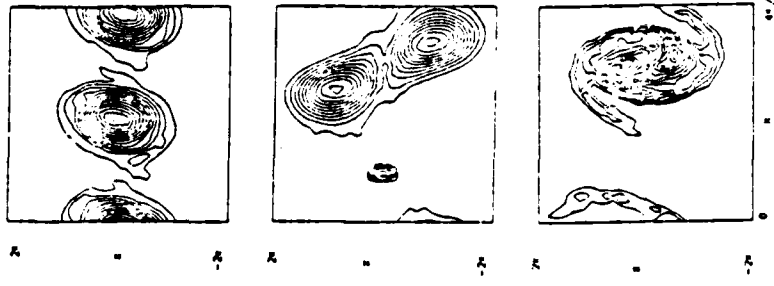


Figure 4.

Spanwise vorticity contours at $t = 48, 72, 96$ during a vortex pairing run with $R = 200$, $V_0(2) = \tanh 2$, $A_{10} = 0.25$, $A_{1/2,0} = 3 \times 10^{-5}$, $W = 16$, $N = 1$, $P = 32$, (resolution $32 = 1 \times 32$), $\alpha = 0.43$, $\alpha_1 = 0.01$.

While these conclusions are in substantial agreement with those

obtained by Kelly (1967) using perturbation theory, they differ in some important respects. First, we observe nothing very special about the resonant wavenumber $\alpha \approx 0.44$ of maximum linear growth presumably because our study is a temporal, not spatial, stability analysis. Second, we do not find that the growth rate of the pairing mode is significantly enhanced by the finite-amplitude primary mode (Pierrehumbert & Widnall 1982). On the contrary, the growth rate of the pairing mode at $1/2\alpha = 0.22$ seems to be slightly less when the primary achieves finite amplitude than for the parallel shear flow.

The saturated two-dimensional flow is also subject to three-dimensional instabilities. While the laminar mean flow is inviscidly unstable only for $\alpha^2 + \beta^2 < 1$, the finite-amplitude two-dimensional flow can be unstable for large α at high R . In Fig. 6, we plot the evolution of three-dimensional disturbance energy

$$E_{3D} = \sum_m E_{m1}(t) \quad (3.5)$$

for runs with initial conditions (3.1) with $A_{10} = 0.25$, $A_{1/2,0} = 0$, $A_{11} = 10^{-6}$ with $\alpha = 0.4$, $\beta = 0.8$. For these parameter values, the mean flow is both viscously and inviscidly stable at these three-dimensional scales. Nevertheless, the saturated two-dimensional disturbed flow is strongly unstable at these scales with disturbances growing at roughly the same rate as the inviscid two-dimensional primary instability. Since the two-dimensional modes saturate, the three-dimensional modes can achieve finite amplitudes on convective time scales and thereby modify significantly the later evolution of the flow.

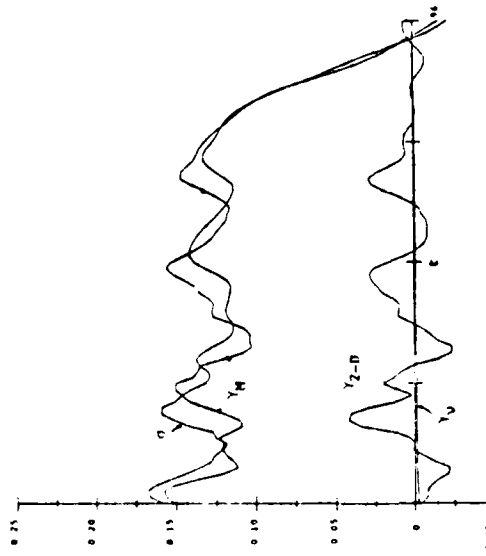


Figure 5
A plot of the components Y_M , Y_D , Y_V (see (3.4)) of the growth rate of the pairing mode amplitude as functions of time for the same run as in Figure 4.

The growing three-dimensional wave is localized in space on top of the two-dimensional vortex motion. In Fig. 7, a plot is given of contours of the spanwise (three-dimensional) perturbation velocity $v(x, z, t)$, as well as a wind plot of the finite amplitude two-dimensional flow $(u(x, 0, z, t), w(x, 0, z, t))$. The structure of this three-dimensional mode is not dissimilar to that found in wall bounded flow (see Orszag & Patera 1983 for a detailed discussion of these latter modes).

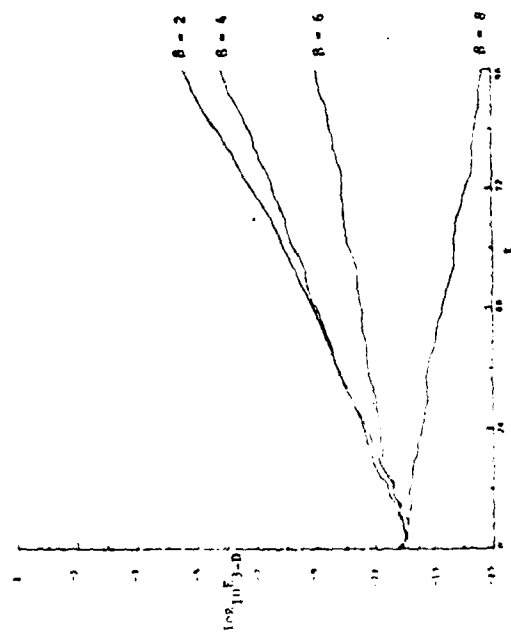


Figure 6.
A plot of the evolution of the three-dimensional disturbance energy $E_3(D)$ vs t for runs with $R = 400$, $U_0(r) = \tanh r$, $M = 6$, $N = 4$, $P = 32$ (resolution $\theta = 4 \times 32$), $\alpha = 0.4$, $\Delta t = 0.02$, $A_{10} = 0.25$, $A_{11} = 10^{-6}$, and $\beta = 2, 4, 6, 8$.

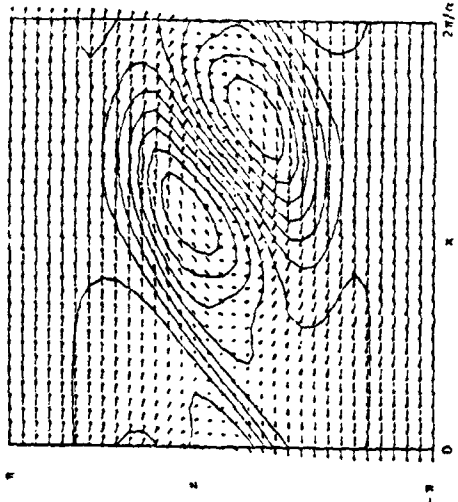


Figure 7.

Contour plot of the perturbation three-dimensional velocity component $v(z,0,2,11)$ in the plane $y = 0$ superimposed on a wind (vector) plot of the finite amplitude vortex flow ($z(t), 0, 2, 11$, $w(z,0,2,11)$) whose velocity contours are plotted in Figure 2. Here $R = 200$, $W = 0.8$, $B = 0.8$, $U_0(r) = \tanh r$, $M = N = P = 32$, resolution $32 \times 32 \times 32$ with no pairing modes, and the contours are plotted at 1×24 .

In Fig. 8, a plot of the average three-dimensional growth rate $\sigma_3 D$ vs β is given for various R when $\alpha = 0.4$. It is apparent from the results plotted in Fig. 8 that, as R increases, $\sigma_3 D$ approaches a finite limit for fixed β (so the secondary instability discussed is inviscid in character) and that the instability turns off for $\beta > \beta_{\text{crit}} = 1/3\sqrt{R}$.

The cutoff β_{crit} is due to viscous damping as nonlinear transfers very little with β . This point is established in Fig. 10 where we plot the contributions to the growth rate $\sigma_3 D$:

$$\frac{1}{2}E_{3-D} - \frac{1}{dt} = \gamma_M + \gamma_{2-D} + \gamma_V \quad (1.6)$$

where γ_M involves the nonlinear interaction of the three-dimensional and mean flows, γ_{2-D} the interaction of the three-dimensional and two-dimensional disturbances, and γ_V the viscous dissipation of three-dimensional energy. It is apparent from Fig. 10a that, for $\beta < \beta_{\text{crit}}$, $\gamma_V - \gamma_{3-D} < \gamma_M$, so the three-dimensional modes derives its energy from the mean flow with the two-dimensional disturbance acting as a catalyst for this transfer.

On the other hand, the results plotted in Fig. 10b show that when $\beta > \beta_{\text{crit}}$, γ_V is quite significant. The three-dimensional instability seems to be turned off at large cross-stream wavenumber β by increasing dissipation rather than by any significant qualitative change in nonlinear transfers from the mean and two-dimensional components.

The flows that develop from the three-dimensional secondary instability do not saturate in ordered states like those of the primary two-dimensional and pairing instabilities. Instead, the three-dimensional modes seem to lead to chaos and, finally, turbulence. In Figs. 11, contour plots of spanwise vorticity and wind profiles in three-dimensional mixing layer runs (at resolution $M = N = P = 32$) are given at $t = 36$ after the three-dimensional fluctuations

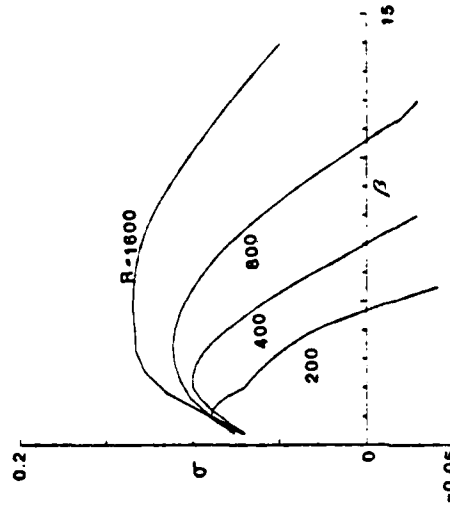


Figure 8.

A plot of the computed three-dimensional growth rate $\sigma_3 D$ (see (3.6)) as a function of spanwise wavenumber β for various Reynolds numbers for $U_0(z) = \tanh z$. Here $\alpha = 0.4$.

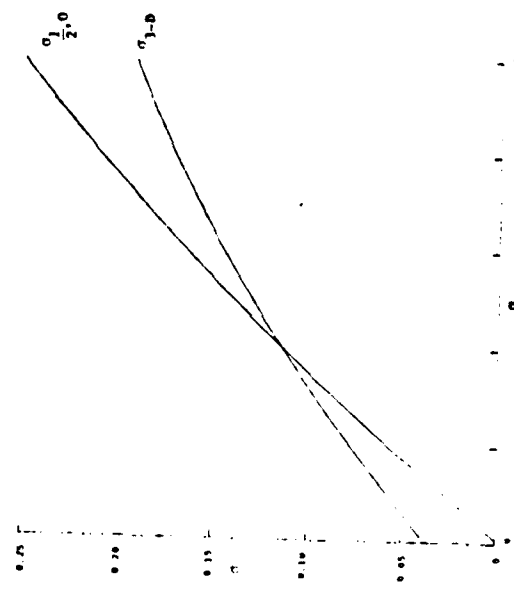


Figure 9

A plot of the computed pairing growth rate $\alpha_{1,0}$ and three-dimensional growth rate $\alpha_{3,D}$ as a function of α at $R = 400$. $\beta = 0.6$ with $U(12) = \tanh \beta$ (Note that the wavenumber of the pairing mode is $\sqrt{\alpha}$)

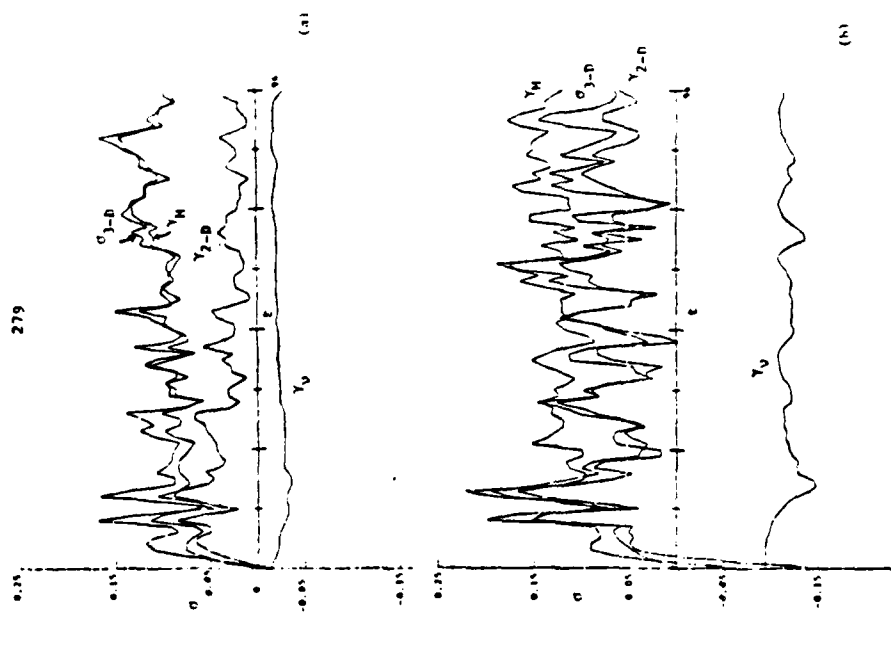


Figure 10

A plot of the components $\tau_{1,0}$, $\tau_{2,0}$, τ_3 (see (3.61) of the three-dimensional growth rate $\alpha_{3,D}$ as functions of time for $R=400$, $\alpha = 0.4$, $A_{10} = 0.25$, $A_{11} = 10$, (a) $\beta = 4$ (b) $\beta = 6$

become comparable to the two dimensional amplitudes. The order apparent in Fig. 7 is partially obliterated by the three dimensional excitations apparent in Fig. 11, but two dimensional structure is still significant.

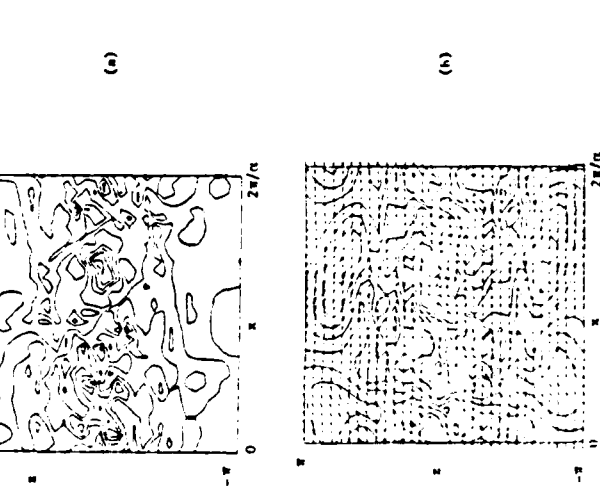


Figure 11

(a) Contour plot of spanwise vorticity in the plane $y = 0$ at $t = 36$ for the run described in the caption to Figure 7. (b) Contours of spanwise velocity v and wind plot of (u, w) vector field in the plane $y = 0$ at $t = 36$ for the run described in the caption to Figure 7.

The nature of the competition between two dimensional pairing and three dimensional instability is further illustrated by the results plotted in Figs. 12, 13 in both figures, results of runs with $\alpha = 400$, $\alpha = 0.4$, $\theta = 0.2$ are plotted. In Fig. 12, the initial conditions are chosen so that the pairing mode perturbation is much larger than that of the three dimensional perturbation. It seems that the pairing process slightly inhibits the three dimensional instability. In Fig. 13, the evolution of the instabilities are plotted when the initial three dimensional perturbation is much larger than the pairing mode. In this case, it seems that the pairing instability is nearly unaffected by the three dimensional instability before finite amplitudes are reached: when the three dimensional mode becomes finite in amplitude, the flow is chaotic so a higher resolution three dimensional code should be used to study the energetics.

5. Discussion

The principal result of this paper is the demonstration that small scale three dimensional instabilities like those previously studied by Orsier & Peters (1980, 1981, 1982), Pierrehumbert & Widnall (1982) exist in viscous free shear flows and that these instabilities persist in moderately low Froude number. It is possible that these modes are responsible for the initial development of three dimensionality in these shear flows. The dynamics of the three dimensional instability is qualitatively the same as that of the three dimensional instabilities studied by us in wall bounded shear flows. In particular, the instability does not appear to be similar to the Coriolis instability in curved channels: as the instability has significant streamwise variation along the two dimensional eddy, while the instability shares some features of a classical *infection*ed instability, including phase locking with the primary vortex. Inflectional instability is preferentially

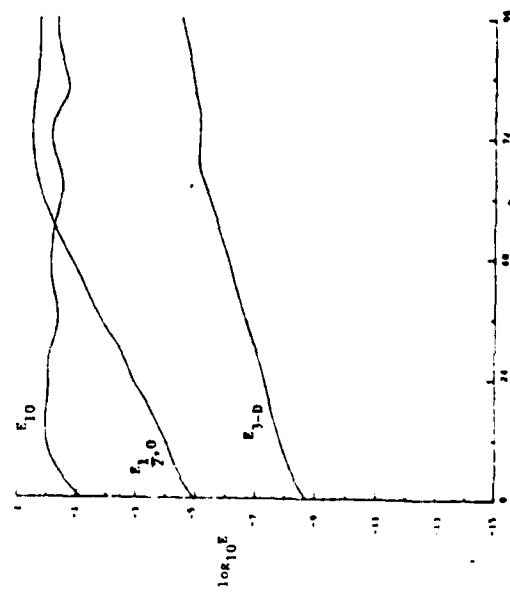


Figure 12

A plot of the evolution of the energies E_{10} , E_{3-0} , E_{3-D} , E_{7-0} , and E_{7-D} vs t for a run with $R = 400$, $U(12) = \tanh z$, $\alpha = 0.4$, $\beta = 0.2$, $M = 8$, $N = 4$, $P = 32$, and initial conditions $A_{10} = 0.25$, $A_{3-0} = 4$, $A_{3-D} = 10^{-3}$, $A_{7-0} = 3.3 \times 10^{-5}$, $A_{7-D} = 0$. The subharmonic pairing mode dominates the three-dimensional mode.

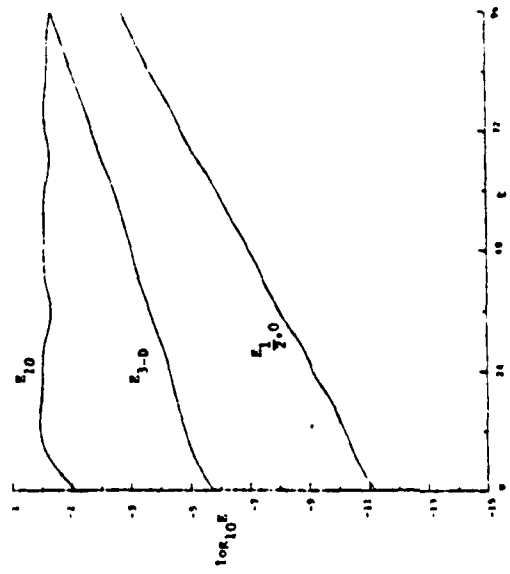


Figure 13

Same as Figure 12, except that the initial conditions are $A_{10} = 0.25$, $A_{3-0} = 3 \times 10^{-6}$, $A_{3-D} = 10^{-3}$. The three-dimensional mode initially dominates the pairing mode.

two dimensional but the present instability is not.

It seems that the mechanics of transition in the free shear flows studied here may, in a sense, be rather more complicated than in the case of well bounded shear flows. In the latter case, linear instabilities are often viscously driven and, therefore, weak, so they can not be directly responsible for the rapid distortions characteristic of transition. On the other hand, free shear flows are subject to a variety of inviscid instabilities so there may be many paths to turbulence. The choice of which path is taken in any individual flow may depend on the results of competition between primary, subharmonic, and three dimensional instabilities, all of which are convectively driven and, therefore, strong with comparable growth rates. Thus, it may be that the evolution of free shear flows in transitional regions may depend significantly on the past history of the flow, including the mechanism of its generation and the external environment in which the flow is embedded.

This work was supported by the Office of Naval Research under contract N00014 82 C 0451, the National Science Foundation under grant ATM-841410, and the Air Force Office of Scientific Research grants contract F49620 85 C 0026. The computations reported here were performed at the Computing Facility of the National Center for Atmospheric Research, Boulder CO, which is supported by the National Science Foundation.

References

Hornal, L.P., Freidenthal, R.E., Brown, G.L., Konrad, J.H., & Poinard, A. 1979 On the development of three dimensional small scales in turbulent mixing layers. In *Proc. 2nd Int. Symp. on Turbulent Shear Flows*, Imperial College, London.

Brachet, M.F., Melton, D.L., Orzaes, S.A., Nickel, R.G., Mori, R.H. & Frisch, U. 1983 Small Scale structure of the Taylor-Green vortex. *J. Fluid Mech.* 130, 411-452.

Broward, F.K. & Trouw, T. 1980 A note on spanwise structure in the two dimensional mixing layer. *J. Fluid Mech.* 97, 771.

Brown, G.L. & Fofsha, A. 1974 On density effects and large structures in turbulent mixing layers. *J. Fluid Mech.* 64, 775.

Collins, D.A. 1992 A numerical study of the stability of a stratified mixing layer. Ph.D. Thesis, Department of Mathematics, McGill Univ., Montreal.

Davidson, M.O., Israel, M. & Orzaes, S.A. 1983 Splitting methods for incompressible flow problems. To be published in *Drizin, R.G. & Reid, W.H. 1981 Hydrodynamic Stability*, Cambridge University Press.

Ho, C.M. & Huang, T.S. 1982 Subharmonics and vortex merging in mixing layers. *J. Fluid Mech.* 119, 443-473.

Mihail, R.W. 1972 Experiments on the nonlinear states of free shear layer transition. *J. Fluid Mech.* 56, 645.

Orszag, S.A. & Peters, A.T. 1980 Subcritical transition to turbulence in plane channel flows. *Phys. Rev. Lett.* 45: 989

Orszag, S.A. & Peters, A.T. 1981 Subcritical transition to turbulence in planar shear flows. In *Transition and Turbulence* (ed. R.F. Maynard). Academic, New York

Orszag, S.A. & Peters, A.T. 1983 Secondary instability of wall-bounded shear flows. *J. Fluid Mech.* In press

Patank, P.C. & Sherman, F.S. & Corcos, G.M. 1976 A numerical simulation of Kelvin-Helmholtz waves of finite amplitude. *J. Fluid Mech.* 73: 215.

Pierrehumbert, R.T. & Widnall, S.E. 1982 The two- and three-dimensional instabilities of a spatially periodic shear layer. *J. Fluid Mech.* 110: 59.

Pilley, J.J. & Melcette, R.W. 1980 Direct numerical simulation of a perturbed, turbulent mixing layer. *AIAA Paper No. 80-0274*.

Stuart, J.T. 1987 On finite amplitude oscillations in laminar mixing layers. *J. Fluid Mech.* 29: 417

Wintant, C.D. & Brown, F.K. 1974 Various pairing mechanisms of turbulent mixing layer growth at moderate Reynolds number. *J. Fluid Mech.* 63: 297

Wygnanski, I. Oster, D. Felder, H. & Ohlomeir, R. 1979 On the persistence of quasi two dimensional eddy structure in a turbulent mixing layer. *J. Fluid Mech.* 93: 325

TURBULENT FLOW SIMULATION: FUTURE NEEDS

by

Jean L. Ferziger
 Department of Mechanical Engineering
 Stanford University
 Stanford, CA

I. Introduction

A classification of approaches to the simulation of turbulent flows according to the kind of averaging employed was given by Kline et al. (1978). This paper, concerns three types of methods: ones based on time or ensemble-averaged equations, large eddy simulation, and full simulation. Other methods are important but will not be dealt with.

Full turbulence simulation (FTS) solves the Navier-Stokes equations without modeling and is applicable only to low Reynolds number flows. Large eddy simulation (LES) employs models for the small scales while simulating the large scales. Its advantage over full simulation is its ability to handle a wider variety of flows and higher Reynolds numbers; its principal disadvantage is its reliance on models. Full simulation should be used whenever possible and large eddy simulation when necessary.

Methods based on one-point averages of the Navier-Stokes equations are the best choice for predicting turbulent flows in complex geometries at present. However, the turbulence models used in these methods need to be carefully monitored. They are not as robust as one would like; however, they are often blamed for errors due to numerical methods. FTS and LES cannot be applied directly to simulation of engineering flows and, for the foreseeable future, will be useful in engineering principally for their application to testing models used in the one-point average equations.

This paper will explore the accomplishments of these methods and the problems that need to be solved to extend their usefulness. Needs include better models and numerical

Positive- and negative-effective-viscosity phenomena in isotropic and anisotropic Beltrami flows

B. J. Bayly and V. Yakhot

Program in Applied and Computational Mathematics, Princeton University, Fine Hall, Princeton, New Jersey 08544

(Received 23 December 1985)

A field-theoretic approach, analogous to Kraichnan's direct-interaction approximation, to the stability theory of complex three-dimensional flows is developed. The long-wavelength stability of a class of Beltrami flows in an unbounded, viscous fluid is considered. We examine two flows in detail, to illustrate the effects of strong isotropy versus strong anisotropy in the basic flow. The effect of the small-scale flow on the long-wavelength perturbations may be interpreted as an effective viscosity. Using diagrammatic techniques, we construct the first-order smoothing and direct-interaction approximations for the perturbation dynamics. It is argued that the effective viscosity for the isotropic flow is always positive, and approaches a value independent of the molecular viscosity in the high-Reynolds-number limit; this flow is thus stable to long-wavelength disturbances. The anisotropic flow has negative effective viscosity for some orientations of the disturbance, and is therefore unstable, when its Reynolds number exceeds $\sqrt{2}$.

I. INTRODUCTION

One of the most intriguing problems in the theory of hydrodynamic turbulence is the formation of large-scale structures in a liquid performing random (turbulent) motion at small scales. It is natural to explain the spontaneous formation of large-scale structures as a manifestation of a long-wavelength instability of the corresponding small-scale flow. In a theoretical approach to the description of this phenomenon, it is convenient to assume that the small-scale flow is driven by an external force field which varies with respect to the space coordinates. A previous paper¹ treated the long-wavelength stability of two-dimensional, periodic eddy systems, driven by appropriate steady forces; it was shown that the large-scale instability is likely to occur only if the small-scale flow is sufficiently anisotropic.

In this paper we shall consider small-scale flows of the following form:

$$\mathbf{v}(\mathbf{x}) = \sum_{\hat{Q} \in W} A(\hat{Q})(\hat{u} + i\hat{Q} \times \hat{u})e^{i\hat{Q} \cdot \mathbf{x}/L}, \quad (1.1)$$

where W is a finite set of unit vectors which contains $-\hat{Q}$ whenever it contains \hat{Q} . The velocity field is guaranteed to be real by requiring that the Fourier amplitudes A satisfy $A(-\hat{Q}) = A^*(\hat{Q})$ for each $\hat{Q} \in W$. The vector \hat{u} is a unit vector orthogonal to \hat{Q} . For our purposes it is unnecessary to specify just which vector \hat{u} is chosen out of the unit circle of candidates; changing the choice of \hat{u} is equivalent to changing the phase of the corresponding amplitude A , which turns out to be irrelevant to the long-wavelength stability results. $2\pi L$ is the fundamental period of each Fourier component.

The flows (1.1) have the particular property that the vorticity vector is everywhere a constant scalar multiple of the velocity vector (we shall call this the strong Beltrami property, as opposed to the weak Beltrami property, in which the vorticity is a nonconstant scalar multiple of

the velocity). This means that the nonlinear term in the Navier-Stokes equations reduces to the gradient of a scalar, which can be absorbed into the pressure field. Thus, any velocity field of the form (1.1) is a nontrivial exact steady solution of the Euler equations. Alternatively, we can think of the flow (1.1) as an exact steady flow of a viscous fluid maintained by an externally imposed body force $\mathbf{f} = (\rho v/L^2)\mathbf{v}$, where v is the kinematic viscosity of the fluid.

From the class (1.1) of Beltrami flows, we shall select two for explicit calculations. To observe the effects of extreme anisotropy in the basic state, we shall consider the simple flow obtained when W contains only two wave vectors $\pm\hat{Q}$, which can be chosen to be $(\pm 1, 0, 0)$. With the choice $\hat{u} = (0, 1, 0)$ and real amplitude $A(\pm\hat{Q}) = U_{\text{rms}}/2$, the flow is

$$\mathbf{v} = U_{\text{rms}}(0, \cos(x/L), -\sin(x/L)), \quad (1.2)$$

which has the form of a monochromatic, circularly polarized wave. For the opposite extreme of highly isotropic flow, let us choose W to consist of a large number N of unit vectors \hat{Q} distributed isotropically over the unit sphere. The complex amplitudes $A(\hat{Q})$ are all given modulus $U_{\text{rms}}/\sqrt{2N}$; the phases of $A(\hat{Q})$ are immaterial, and may be chosen randomly. In either case, U_{rms} is the root-mean-square fluid velocity, and is held fixed as N is varied to obtain different degrees of isotropy. Beltrami flows of this type have been used extensively in simulations of diffusion in helical turbulence,² but the present work appears to be the first investigation of their dynamical properties.

The possibility that a small-scale flow with nonzero average helicity might be unstable to the growth of long-wavelength disturbances has been discussed by a number of authors. Moffatt³ has shown that a certain very symmetric Beltrami flow with six Fourier components, known as the Arnol'd-Beltrami-Childress (ABC) flow, is inviscidly unstable to large-scale disturbances with the same sign

of helicity (i.e., the same "handedness") as the basic flow, and Moisseyev *et al.*⁶ have shown that, in a highly compressible fluid, any small-scale turbulent flow with nonzero helicity can support a growing large-scale secondary flow. The purpose of the present paper is to perform an investigation of the possibility of long-wave instability in viscous, incompressible flow, which is typically the situation of greatest physical interest. It is our suspicion that under these conditions, most nontrivial Beltrami flows are stable, and as such may occur and persist in a large variety of turbulent flows.^{7,8}

In this paper, we consider the behavior of long-wavelength disturbances to viscous Beltrami flows, which we assume are maintained by steady external body forces. The perturbation is expanded in powers of the Reynolds number of the basic flow, and we evaluate each term in the long-wave limit. This expansion is essentially the same as the expansion for the long-wave behavior of the averaged impulse-response tensor in a fully turbulent flow, for which Kraichnan originally developed the so-called direct-interaction approximation (DIA). The DIA, as usually used in turbulence theory, consists of an equation for the impulse-response tensor, coupled with an equation giving the evolution of the velocity-velocity correlation function. In this paper, the basic flow is known exactly, so we do not need the auxiliary equation for the velocity autocorrelation. The resulting system is considerably simpler to analyze than most applications of the DIA. We construct both the first-order smoothing and direct-interaction approximations and examine their implications for the two flows described above.

In the long-wave approximation, the growth or decay rate of a large-scale perturbation is a quadratic function of the wave number of the perturbation. For this reason, the effect of the small-scale flow on the evolution of long-wave disturbances may be interpreted as the action of a tensor effective viscosity. In the case of the simple Beltrami flow (1.2) with two Fourier components, only the first nontrivial diagram survives in the long-wave limit for any finite Reynolds number, and the first-order smoothing approximation correctly determines the exact evolution of large-scale perturbations. The effective viscosity is anisotropic, and is actually negative for some orientations of the perturbation. It turns out that large-scale perturbations of suitable orientation are capable of growing on the flow (1.2) when its Reynolds number exceeds $\sqrt{2}$.

For almost isotropic Beltrami flows at low Reynolds numbers, first-order smoothing theory indicates that the viscous damping of long-wave disturbances is enhanced by the reaction of the basic flow, the effective viscosity being isotropic and positive in this case. At finite Reynolds number, however, all terms in the expansion are nominally of the same order in the long-wave limit, and first-order smoothing no longer remains applicable. The solution of the direct-interaction approximation for these flows indicates that the effective viscosity increases with the Reynolds number, eventually approaching a value independent of the molecular viscosity in the limit of infinite Reynolds number. This result supports the conjecture that a large class of Beltrami flows with nontrivial topo-

gies are stable, and might be observed in experiments or numerical simulations.

II. FORMULATION OF THE LONG-WAVE STABILITY PROBLEM

The equations of motion for a viscous fluid in the presence of a steady, quasiperiodic force field are most conveniently used in dimensionless form. Using L as the length scale and v/L as the velocity scale, the dimensionless Navier-Stokes equations take the form

$$\mathbf{v}_t + R \mathbf{v} \cdot \nabla \mathbf{v} = -\nabla p + \nabla^2 \mathbf{v} + \mathbf{f},$$

$$\nabla \cdot \mathbf{v} = 0,$$
(2.1)

where

$$\mathbf{f}(\mathbf{x}) = \sum_{\hat{\mathbf{Q}} \in \mathbf{W}} \mathbf{F}(\hat{\mathbf{Q}}) e^{i\hat{\mathbf{Q}} \cdot \mathbf{x}}, \quad \mathbf{F}(\hat{\mathbf{Q}}) = \mathbf{A}(\hat{\mathbf{Q}})(\hat{\mathbf{a}} + i\hat{\mathbf{Q}} \times \hat{\mathbf{a}}),$$
(2.2)

and the $|\mathbf{A}(\hat{\mathbf{Q}})|$, now dimensionless, have been scaled with respect to the root-mean-square fluid velocity U_{rms} . R is the Reynolds number based on U_{rms} , L , and v . Henceforth, unless explicitly stated, we shall work exclusively with the nondimensional quantities as defined here.

If we define the four-dimensional Fourier transforms of space-time-dependent quantities by

$$a(\mathbf{k}, \omega) \equiv \int \frac{d\mathbf{x} dt}{(2\pi)^4} e^{-i(\mathbf{k} \cdot \mathbf{x} - \omega t)} a(\mathbf{x}, t),$$

$$a(\mathbf{x}, t) \equiv \int d\mathbf{k} d\omega e^{i(\mathbf{k} \cdot \mathbf{x} - \omega t)} a(\mathbf{k}, \omega),$$
(2.3)

then we can write the Navier-Stokes equations as

$$v_i(\mathbf{k}, \omega) = G^0(\mathbf{k}, 0) f_i(\mathbf{k}) \delta(\omega)$$

$$+ G^0(\mathbf{k}, \omega) (-\frac{1}{2} i R) P_{ijl}(\mathbf{k})$$

$$+ \int d\mathbf{q} d\sigma v_j(\mathbf{q}, \sigma) v_l(\mathbf{k} - \mathbf{q}, \omega - \sigma). \quad (2.4)$$

Here $G^0(\mathbf{k}, \omega) \equiv (-i\omega + k^2)^{-1}$ is the so-called zero-order propagator, and

$$P_{ijl}(\mathbf{k}) \equiv k_j(\delta_{ij} - k_i k_j / k^2) + k_l(\delta_{ij} - k_i k_l / k^2).$$

The tensor P_{ijl} incorporates the pressure field and the incompressibility constraint, allowing us to replace the two equations (2.1) by only one (2.4).

The Fourier transform of the force is a sum of δ functions:

$$f_i(\mathbf{k}) = \sum_{\hat{\mathbf{Q}} \in \mathbf{W}} F_i(\hat{\mathbf{Q}}) \delta(\mathbf{k} - \hat{\mathbf{Q}}). \quad (2.5)$$

The Beltrami property of the basic flow implies that the nonlinear term

$$P_{ijl}(\mathbf{k}) \int d\mathbf{q} f_j(\mathbf{q}) f_l(\mathbf{k} - \mathbf{q})$$
(2.6)

vanishes identically, and the basic flow therefore takes the form

$$\mathbf{v}(\mathbf{k}) = G^0(\mathbf{k}, 0) \mathbf{f}(\mathbf{k}) \delta(\omega).$$

an infinitesimal perturbation $v'_i(\mathbf{k}, \omega)$ to the flow

$$v_i(\mathbf{k}, \omega) = G^0(\mathbf{k}, 0)f_i(\mathbf{k})\delta(\omega) + v'_i(\mathbf{k}, \omega) \quad (2.7)$$

and consider its evolution according to the linearized equation

$$v'_a(\mathbf{k}, \omega) = G^0(\mathbf{k}, \omega)(-iR)P_{abc}(\mathbf{k}) \times \int d\mathbf{q} G^0(\mathbf{q}, 0)f_b(\mathbf{q})v'_c(\mathbf{k} - \mathbf{q}, \omega). \quad (2.8)$$

Because of the coupling between the perturbation and the small-scale basic flow, a pure long-wave perturbation is impossible, but we can formally separate the perturbation into long- and short-wave components:

$$v'_a(\mathbf{k}, \omega) = G^0(\mathbf{k}, \omega)(-iR)P_{abc}(\mathbf{k}) \int d\mathbf{q} G^0(\mathbf{q}, 0)\langle f_b(\mathbf{q})v'_c(\mathbf{k} - \mathbf{q}, \omega) \rangle, \quad (2.11a)$$

$$v'_c(\mathbf{k}, \omega) = G^0(\mathbf{k}, \omega)(-iR)P_{cde}(\mathbf{k}) \int d\mathbf{q} G^0(\mathbf{q}, 0)f_d(\mathbf{q})v'_e(\mathbf{k} - \mathbf{q}, \omega) + G^0(\mathbf{k}, \omega)(-iR)P_{cde}(\mathbf{k}) \int d\mathbf{q} G^0(\mathbf{q}, 0)[f_d(\mathbf{q})v'_e(\mathbf{k} - \mathbf{q}, \omega) - \langle f_d(\mathbf{q})v'_e(\mathbf{k} - \mathbf{q}, \omega) \rangle]. \quad (2.11b)$$

The short-wave component can be expressed in terms of the long-wave component by formally iterating (2.11b), which yields an expression in the form of a perturbation series in powers of the Reynolds number of the basic flow. When this series substituted into (2.11a), we obtain an equation involving only the long-wave component of the perturbation, which determines the evolution of the entire perturbation. The analysis of this equation occupies the rest of the paper.

III. FIRST-ORDER SMOOTHING

The first-order smoothing approximation consists of taking only one iteration of the short-wave equation (2.11b) before substituting the result back into the long-wave equation. This amounts to taking the first term in the Reynolds-number expansion of the evolution equation, so the results will be strictly valid only for small Reynolds number. In this regime, the molecular viscosity dominates the inertial processes, so all disturbances are damped. Nevertheless, we can observe whether the small-scale flow tends to enhance or diminish the dissipation, and this information will give us some indication of the situation at higher Reynolds numbers.

The first iteration of (2.11b) yields

$$v'_c(\mathbf{k}, \omega) = G^0(\mathbf{k}, \omega)(-iR)P_{cde}(\mathbf{k}) \int d\mathbf{q} G^0(\mathbf{q}, 0)f_d(\mathbf{q})v'_e(\mathbf{k} - \mathbf{q}, \omega). \quad (3.1)$$

Substituting into (2.11a) then gives an appropriate equation of motion for the long-wave component alone:

$$v'_a(\mathbf{k}, \omega) = G^0(\mathbf{k}, \omega)(-iR)P_{abc}(\mathbf{k}) \int d\mathbf{q}^1 G^0(\mathbf{q}^1, 0)f_b(\mathbf{q}^1)G^0(\mathbf{k} - \mathbf{q}^1, \omega)(-iR)P_{cde}(\mathbf{k} - \mathbf{q}^1) \times \int d\mathbf{q}^2 G^0(\mathbf{q}^2, 0)f_d(\mathbf{q}^2)v'_e(\mathbf{k} - \mathbf{q}^1 - \mathbf{q}^2) = -R^2 G^0(\mathbf{k}, \omega)P_{abc}(\mathbf{k}) \sum_{\hat{\mathbf{Q}} \in \mathcal{W}} G^0(\mathbf{k} - \hat{\mathbf{Q}}^1, \omega)P_{cde}(\mathbf{k} - \hat{\mathbf{Q}}^1)F_b(\hat{\mathbf{Q}}^1)F_d(\hat{\mathbf{Q}}^2)v'_e(\mathbf{k} - \hat{\mathbf{Q}}^1 - \hat{\mathbf{Q}}^2, \omega) \quad (3.2)$$

after performing the \mathbf{q} integrals. But $v'_e(\mathbf{k} - \hat{\mathbf{Q}}^1 - \hat{\mathbf{Q}}^2, \omega)$ is nonzero only if $\hat{\mathbf{Q}}^2 = -\hat{\mathbf{Q}}^1 + O(\epsilon)$, which implies $\hat{\mathbf{Q}}^2 = -\hat{\mathbf{Q}}^1$, because there is only a finite number of distinct wave vectors in \mathcal{W} and we are interested in the limit $\epsilon \rightarrow 0$. Therefore,

$$v'_a(\mathbf{k}, \omega) = -R^2 G^0(\mathbf{k}, \omega)P_{abc}(\mathbf{k}) \sum_{\hat{\mathbf{Q}} \in \mathcal{W}} G^0(\mathbf{k} - \hat{\mathbf{Q}})P_{cde}(\mathbf{k} - \hat{\mathbf{Q}})|A(\hat{\mathbf{Q}})|^2(\delta_{bd} - \hat{Q}_b\hat{Q}_d - i\epsilon_{bdc}\hat{Q}_c)v'_e(\mathbf{k}, \omega), \quad (3.3)$$

where we have used the fact that a helical vector $\mathbf{F}(\hat{\mathbf{Q}}) = A(\hat{\mathbf{Q}})[\hat{\mathbf{u}} + i\hat{\mathbf{Q}} \times \hat{\mathbf{u}}]$ has the property that

$$F_b(\hat{\mathbf{Q}})F_d(-\hat{\mathbf{Q}}) = |A(\hat{\mathbf{Q}})|^2(\delta_{bd} - \hat{Q}_b\hat{Q}_d - i\epsilon_{bdc}\hat{Q}_c), \quad (3.4)$$

regardless of the phase of $A(\hat{\mathbf{Q}})$ or the choice of $\hat{\mathbf{u}}$.

Now, we can simplify (3.3) by taking the limit of small $|\mathbf{k}|$ and using the incompressibility conditions

$$\hat{Q}_a F_a(\hat{\mathbf{Q}}) = 0, \quad k_a v'_a(\mathbf{k}, \omega) = 0. \quad (3.5)$$

where

$$v'_a(\mathbf{k}, \omega) \equiv 0 \text{ if } |\mathbf{k}| > \epsilon, \quad (2.10)$$

$$v'_a(\mathbf{k}, \omega) \equiv 0 \text{ if } |\mathbf{k}| < \epsilon,$$

for some long-wave cutoff $0 < \epsilon \ll 1$. We define the operators $\langle \cdot \rangle$ and $I - \langle \cdot \rangle$ as the projections onto the long- and short-wave subspaces, respectively, of the function space we are working in.

The long- and short-wave projections of the equation of motion (2.8) are then

$$-i\omega = -k^2(1 + \frac{8}{15}R^2). \quad (3.15)$$

The small-scale flow in this case therefore enhances the damping of all long-wave disturbances irrespective of wave-vector direction or polarization, as would be anticipated for such an isotropic small-scale flow. In particular, the isotropic nature of the small-scale flow has eliminated the special directions in which perturbations were amplified or only weakly damped.

IV. HIGHER-ORDER THEORY: DIAGRAM EXPANSION AND DIA

Because of the complexity of the algebraic manipulations, we shall use diagrammatic notation for analyzing the perturbation equations (2.11). The procedure is standard, but we shall present the derivations in detail for the sake of completeness. Let the thin line represent the zero order propagator G^0 , the cross denote the force f , and the vertex the quantity $(-iR)P$, with indices to be specified later. Also, let the open bar represent the long-wave part of the perturbation, and the slashed open bar the short-wave part. These symbols are drawn in Figs. 1(a)–1(e), respectively.

Equations (2.11a) and (2.11b) can then be represented by the diagrams in Figs. 2(a) and 2(b). Each vertex has a line exiting on the left, a line entering from the right, and a line entering from the upper right, whose other end consists of a force term. Each of these lines possesses a wave vector and an index, which must agree with the wave vector and index at the force or vertex at each of its ends. At each vertex, the wave vector on the left must equal the sum of the right wave vector and the slanted force wave vector. All repeated indices are summed over, and all internal wave vectors are integrated, resulting in wave-vector sums of the same form as (2.13). Since the vertex



FIG. 1. Constituents of diagrams.

contains a factor of the Reynolds number, a diagram with n vertices corresponds to a quantity proportional to R^n .

The short-wave perturbation may be expressed in terms of the long-wave part by iterating Fig. 2(b). The first two approximations are shown in Fig. 3. Now, the term a in Fig. 3 translates into the algebraic expression

$$-R^2 \sum_{\hat{Q}^1, \hat{Q}^2 \in \mathcal{W}} P_{abc}(\mathbf{k}) G^0(\hat{Q}^1) F_b(\hat{Q}^1) G^0(\mathbf{k} - \hat{Q}^1) \\ \times P_{cde}(\mathbf{k} - \hat{Q}^1) G^0(\hat{Q}^2) F_d(\hat{Q}^2) v_e^<(\mathbf{k} - \hat{Q}^1 - \hat{Q}^2, \omega)$$

and so the only contribution to the long-wave projection b of term a comes from pairs \hat{Q}^1, \hat{Q}^2 that cancel. This can be indicated diagrammatically by replacing the force branches by an arc as in Fig. 4(a).

In general, the long-wave part of a diagram with an odd number of force branches vanishes, and the long-wave part of a diagram with an even number of branches is the sum of all possible diagrams obtained by connecting the branches in pairs. For example, the long-wave parts of the next nontrivial diagram is shown in Fig. 4(b). Long-wave diagrams that can be disconnected by severing one G^0 line are called *reducible* diagrams (labeled r in Fig. 4), and those which cannot (labeled i) are *irreducible*. So as not to count diagrams with internal wave vector \mathbf{k} twice, we require the following rule for evaluating irreducible diagrams: the sum over all wave-vector combinations must exclude those for which one (or more) of the internal wave vectors is \mathbf{k} . So, for instance, the diagram in Fig. 4(c) with the crossed arcs has the value

$$R^4 \sum_{\hat{Q}^2 = -\hat{Q}^1} G^0(\mathbf{k}, \omega) P_{abc}(\mathbf{k}) F_b(\hat{Q}^1) G^0(\mathbf{k} - \hat{Q}^1, \omega) P_{cde}(\mathbf{k} - \hat{Q}^1) F_d(\hat{Q}^2) \\ \times G^0(\mathbf{k} - \hat{Q}^1 - \hat{Q}^2, \omega) P_{efi}(\mathbf{k} - \hat{Q}^1 - \hat{Q}^2) F_f(-\hat{Q}^1) G^0(\mathbf{k} - \hat{Q}^2, \omega) P_{ijm}(\mathbf{k} - \hat{Q}^2) F_j(-\hat{Q}^2) v_m^<(\mathbf{k}, \omega).$$

We can now extend the iteration scheme for $v_i^>(\mathbf{k}, \omega)$ to arbitrary order in R . The next approximations are shown in Fig. 5. The two reducible diagrams in Fig. 5(b) cancel, leaving an expression for the fourth approximation that involves only irreducible diagrams. This cancellation of reducible diagrams is quite general, and the full expansion of $v_i^>(\mathbf{k}, \omega)$ is given in Fig. 6. The quantity I_m is the sum of all irreducible diagrams with $2m$ vertices, minus the external legs.

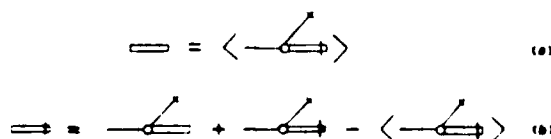


FIG. 2. Equation (2.11) in diagram form.

Having found the expansion of $v_i^>$ in terms of $v_i^<$ we can now substitute it into Fig. 2(a) to find the equation of motion for $v_i^<$ by itself. Only the diagrams in Fig. 6 with an odd number of branches contribute, and all the reducible diagrams cancel in the long-wave projection, leaving the expression in Fig. 7(a). Figure 7(a) can be rewritten in terms of the renormalized vertex $\Sigma_{ab}(\mathbf{k}, \omega)$, defined as the sum of all the legless irreducible diagrams. The resulting equation [Fig. 7(b)], whose algebraic translation is

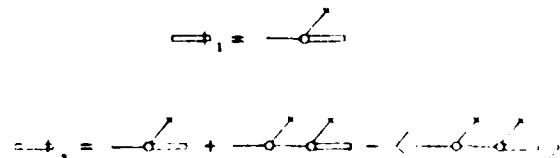


FIG. 3. First two iterations of Fig. 2(b).

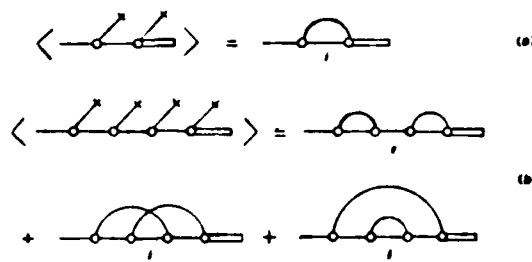


FIG. 4. Long-wave components of simple diagrams.

$$v_a^\zeta(k, \omega) = G^0(k, \omega) \Sigma_{ab}(k, \omega) v_b^\zeta(k, \omega), \quad (4.1)$$

can then be solved provided we can find some sensible approximation for $\Sigma_{ab}(k, \omega)$.

Formally, therefore, we have found the exact form of the Reynolds-number expansion of the long-wave equation of motion. Strictly speaking, the expansion procedure is only valid when $R \ll 1$, in which case we can get a good approximation to the dynamics by taking only the first term in the series. This term, which consists of the single second-order diagram, gives the first-order smoothing approximation that was discussed in the last section. When the Reynolds number ceases to be small, the series in its raw, untreated form is not likely to be useful, and we must resort to more sophisticated methods of series summation.

Consider the subseries, exhibited in Fig. 8(a), of the series defining the vertex function Σ . The sum of the inner parts of these diagrams formally defines a function $G_{ab}(k, \omega)$ called the full propagator, which we denote by a heavy line. Every diagram in Fig. 7(b) belongs to exactly one series analogous to Fig. 8(a) that can be similarly summed, and so the entire series for Σ can be rewritten in terms of G , as in Fig. 8(b). The diagrams remaining in this consolidated series are those whose arcs cannot be divided into two groups such that no member of one group intersects any member of the other.

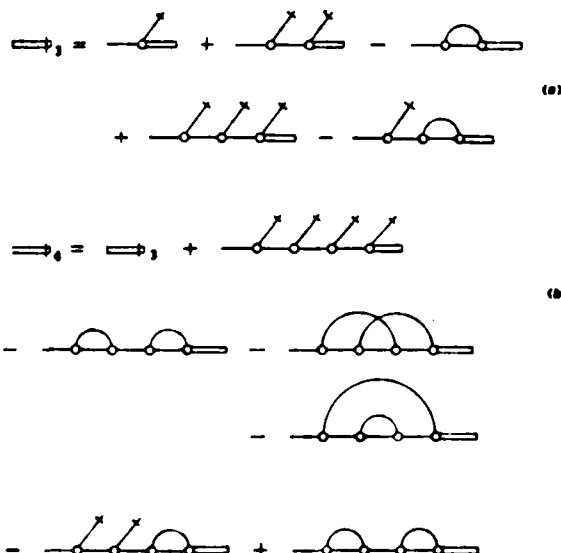


FIG. 5. Third and fourth iterations of Fig. 2(b).

$$\begin{aligned} \Rightarrow &= \text{---} + (1 + \text{---}) \\ &\times \sum_{n=1}^{\infty} \{ \text{---} \dots \text{---} \\ &- \sum_{m=1}^n \text{---} \dots \text{---} \text{---} \text{---} \} \end{aligned}$$

$$\begin{aligned} \text{I}_1 &= \text{---} \\ \text{I}_2 &= \text{---} + \text{---} \\ \text{etc.} & \end{aligned}$$

FIG. 6. Full expansion of short-wave component.

The resummation of Fig. 7(b) has not simplified the problem of calculating Σ at all; rather, we have just transformed the problem of finding Σ into the problem of finding G . But now we can perform the same resummation procedure on the series for G itself, and obtain a consolidated series for G in terms of itself, which can be expressed in closed form in terms of Σ (Fig. 9). This equation, whose algebraic form is

$$G_{ac}(k, \omega) = G^0(k, \omega) \delta_{ac} + G^0(k, \omega) \Sigma_{ab}(k, \omega) G_{bc}(k, \omega),$$

can be inverted:

$$G_{ab}(k, \omega) = [G^{0-1}(k, \omega) - \Sigma(k, \omega)]^{-1} \text{---}_{ab}. \quad (4.2)$$

With G given by (4.2), Σ is now determined as the solution of a nonlinear integral equation, known as the *Dyson equation*. Truncating the Dyson equation and solving the

$$\begin{aligned} \text{---} &= \text{---} + \text{---} \\ &+ \text{---} + \dots \\ \text{---}_a &= \text{---} + \text{---} \\ &+ \text{---} - \text{---} \\ &- \text{---} - \text{---} \\ &- \text{---} - \text{---} \\ &- \text{---} + \text{---} \\ \Sigma &= \sum_{m=0}^{\infty} \text{I}_m = \text{---} \\ &+ \text{---} + \text{---} + \dots \end{aligned}$$

FIG. 7. Dispersion relation for long-wave component

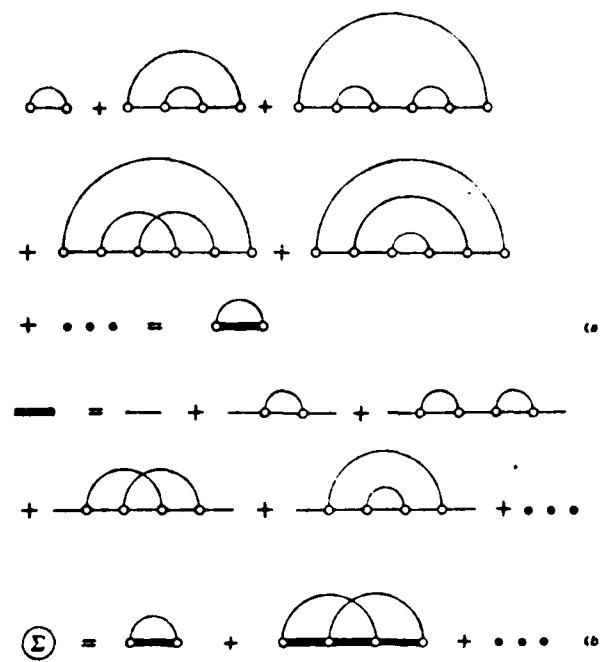


FIG. 8. Resummation of subseries.

resulting closed-integral equation gives a new approximation to the vertex, which may have useful properties that no finite number of terms of the original expansion had.

The DIA for Σ is given by the lowest truncation of the Dyson equation

$$\begin{aligned} \Sigma_{af}(\mathbf{k}, \omega) &= -R^2 P_{abc}(\mathbf{k}) \\ &\times \sum_{\hat{\mathbf{Q}} \in \mathcal{W}} |\mathcal{A}(\hat{\mathbf{Q}})|^2 (\delta_{be} - \hat{\mathbf{Q}}_b \hat{\mathbf{Q}}_e - i \epsilon_{bex} \hat{\mathbf{Q}}_x) \\ &\times G_{cd}(\mathbf{k} - \hat{\mathbf{Q}}, \omega) P_{def}(\mathbf{k} - \hat{\mathbf{Q}}) \quad (4.3) \end{aligned}$$

with G_{ab} given by (4.2). By reexpanding (4.3) in powers of R , it turns out that the DIA simply consists of summing up the subset of the full diagram series that consists of all diagrams whose arcs do not intersect at all. Whether or not the DIA is a good approximation depends on the relative importance of the diagrams with less trivial topological structure; this issue will be discussed in Sec. VI.

V. RESULTS OF HIGHER-ORDER THEORY

For the simple Beltrami flow (1.2), the sum of all the diagrams of a given order n , which is of order R^n by definition, is also of order k^n in the long-wave limit. In this limit, therefore, only the single second-order diagram contributes to the dynamics of the perturbation, and hence

$$\begin{aligned} \Sigma &= \Sigma_{af} + \Sigma_{bf} + \dots \\ &= \Sigma_{af} + \Sigma_{bf} + \Sigma_{cf} \quad (\Sigma) \end{aligned}$$

FIG. 9. Dyson equation for $G_{ab}(\mathbf{k}, \omega)$.

the first-order smoothing approximation is exact for large-scale disturbances to (1.2). The results of Sec. III, in particular the prediction that the flow is unstable if $R > \sqrt{2}$, are consequently valid for all finite Reynolds numbers.

One way to demonstrate this is by an appeal to classical (Orr-Sommerfeld) stability theory. Because the velocity field (1.2) is independent of the y and z coordinates, the instability modes have the exact form

$$\mathbf{v}'(\mathbf{x}, t) = e^{ik_{OS}(x-ct)} (u_{OS}, v_{OS}, w_{OS}),$$

where

$$\mathbf{k}_{OS} = (0, k_2, k_3), \quad \mathbf{c} = (0, c_2, c_3),$$

and u_{OS}, v_{OS}, w_{OS} are functions of x alone. Eliminating v_{OS} and w_{OS} from the linearized Navier-Stokes equations yields an Orr-Sommerfeld equation for $u_{OS}(x)$:

$$\begin{aligned} [U(x) - c] \left[\frac{d^2 u_{OS}}{dx^2} - k_{OS}^2 u_{OS} \right] - \frac{d^2 U(x)}{dx^2} u_{OS} \\ = \frac{1}{ik_{OS} R} \left[\frac{d^2}{dx^2} - k_{OS}^2 \right]^2 u_{OS}, \quad (5.1) \end{aligned}$$

where $k_{OS} = |\mathbf{k}_{OS}|$, and

$$U(x) = \mathbf{k}_{OS} \cdot \mathbf{v}(x) / k_{OS}, \quad c = \mathbf{k}_{OS} \cdot \mathbf{c} / k_{OS}$$

are the components of \mathbf{v} and \mathbf{c} parallel to \mathbf{k}_{OS} .

In the long-wave limit, with finite Reynolds number, the quantity $k_{OS} R$ is small, and (5.1) can be solved to give $u_{OS}(x)$ as a power series in $k_{OS} R$. But this is exactly the same procedure that we followed in Sec. IV, although here we performed more preliminary simplifications before expanding. The series obtained using either formalism must agree at each order in R ; therefore the sum of all the n th-order diagrams in the diagram expansion must equal the coefficient of R^n in the Orr-Sommerfeld expansion, which is proportional to k_{OS}^n . This result can also be demonstrated directly by keeping track of the orders of successive approximations to v_a while iterating (2.11b); we omit this calculation because the details are much more intricate and no more instructive than the Orr-Sommerfeld treatment.

The reason for the simplification of the series appears to be the fact that in a sufficiently regular flow, the long-wave perturbation modes also have regular spatial behavior. The Fourier components of the perturbation decay algebraically with wave number at any Reynolds number; indeed, they decay so rapidly that the component of the disturbance at any wave vector which is the sum of \mathbf{k} and a nonzero combination of two or more basic-flow wave vectors do not participate in the dynamics. There is therefore no transfer of perturbation energy to higher and higher wave numbers, and it is not surprising that the long-wave evolution depends strongly on the molecular viscosity, even in the high-Reynolds-number limit.

For flows with complex spatial structure, the perturbation modes also have very involved spatial structure. In fact, the perturbation is likely to become singular in the limit of infinite Reynolds number. There is no finite set

of terms from the original expansion that satisfactorily describes perturbations to almost-isotropic flows at moderate or high Reynolds number. Even in the long-wave limit, all diagrams in the series [Fig. 8(b)] are nominally of order k^2 , which indicates that components of the perturbation at all length scales are important in the dynamics of the long-wave part. It is reasonable to expect that a cascade may develop at high Reynolds numbers, with perturbation energy from the largest scales being transferred to smaller and smaller scales until it can be efficiently dissipated by viscosity. The damping of long-wave disturbances would then become independent of the molecular viscosity for large Reynolds numbers, and be determined by the velocity and length scales of the flow field alone.

Although the DIA does not involve anything like the complexity of the full series for Σ in Fig. 7, it nonetheless includes some of the structure of the perturbation at arbitrarily small scales. If there is an energy cascade for the perturbation, we may be able to deduce some of its qualitative characteristics by analyzing its DIA equations. The essence of the problem is to solve (4.3) for the renormalized vertex $\Sigma_{ab}(\mathbf{k}, \omega)$. Since the basic flow is isotropic (to an arbitrarily good approximation), the tensors G and Σ have the forms

$$G_{ab}(\mathbf{k}, \omega) = g(k, \omega)(\delta_{ab} - k_a k_b / k^2) - i h(k, \omega) \epsilon_{aby}(k_y / k),$$

$$\Sigma_{ab}(\mathbf{k}, \omega) = \sigma(k, \omega)(\delta_{ab} - k_a k_b / k^2) + i \tau(k, \omega) \epsilon_{aby}(k_y / k),$$

where g , h , σ , and τ are scalar functions that depend on the wave vector \mathbf{k} only through its modulus k .

Since we are primarily interested in the long-time, large-scale behavior of the Green's function, we can simplify the analysis of the integral equations by setting the frequency ω to zero within the integrals; the problem is insensitive to this approximation, and the resulting simplification is enormous. Then, by extracting the symmetric and antisymmetric parts of (4.3), respectively, we can reduce the Dyson equation to a pair of scalar integral equations over the unit sphere, which can in turn be transformed into integrals over the cosine of the angle between \mathbf{k} and $\hat{\mathbf{Q}}$:

$$\begin{aligned} \sigma(k, 0) &= -\frac{1}{4} R^2 \int_{-1}^1 dc \frac{(1-c^2)}{q^2} [\alpha(k, c) g(q, 0) \\ &\quad + \beta(k, c) h(q, 0)], \\ \tau(k, 0) &= -\frac{1}{4} R^2 \int_{-1}^1 dc \frac{(1-c^2)}{q^2} [\gamma(k, c) g(q, 0) \\ &\quad + \eta(k, c) h(q, 0)], \end{aligned} \quad (5.2)$$

where the "kernels" of the integral equations are given by

$$q \equiv q(k, c) \equiv (1 + k^2 - 2kc)^{1/2},$$

$$\alpha(k, c) = 2kc - 4k^3c + 2k^4, \quad \beta(k, c) = 2kc - 2k^2,$$

$$\gamma(k, c) = 4k^2c - 4k^3, \quad \eta(k, c) = 2k^2c - 2k^3.$$

The integral equations (5.3) are "closed" by solving Eq. (4.2) for g and h in terms of σ and τ , which yields the relations

$$g(k, \omega) = [k^2 - \sigma(k, \omega)] / D(k, \omega),$$

$$h(k, \omega) = -\tau(k, \omega) / D(k, \omega)$$

with

$$D(k, \omega) = [k^2 - \sigma(k, \omega)]^2 - \tau(k, \omega)^2.$$

Equations (5.2) and (5.3) can be solved using standard numerical techniques. The functions σ and τ are approximated by specifying their values at a suitable mesh points on the k axis, and linearly interpolating the values for all other points. The integrals (5.3) can then be evaluated at the mesh points using a standard ten-point Gaussian scheme for the c integrals. By performing many-dimensional Newton iteration, we can rapidly find the values of σ and τ at the mesh points which are reproduced by the integration. Successively finer meshes are used until the values for the eddy viscosity (see below) are changed by 1% or less upon doubling the resolution.

It is easily checked that the asymptotic behavior $\sigma(k, 0)$ is quadratic in k as $k \rightarrow 0$, while the asymptotic behavior of $\tau(k, 0)$ is cubic in k . So, although the antisymmetric part of Σ is important for the solution of the integral equation, it does not enter explicitly into the long-wave equation. The behavior of long-wave perturbations is determined by the quantity $\Gamma(R) = \lim_{k \rightarrow 0} [-\sigma(k, 0) / k^2 R]$, which is a nontrivial function of the Reynolds number R . Using Eqs. (4.1) and (5.2), the long-wave dispersion relation is given by

$$-i\omega = -k^2 [1 + R\Gamma(R)], \quad (5.4)$$

or, in the original dimensional units,

$$-i\omega = -k^2 [v + (U_{rms} L) \Gamma(R)]. \quad (5.4)$$

Thus, for large Reynolds number, a long-wave disturbance damps out as if acted on by an effective eddy viscosity $(U_{rms} L) \Gamma(R)$. A plot of $\Gamma(R)$ as a function of Reynolds number is shown in Fig. 10; it should be noted that as R increases, Γ tends rapidly to a finite asymptotic value confirming the hypothesis that at high Reynolds number the exact value of the molecular viscosity is unimportant for the dynamics. The straight line through the origin has slope $\frac{1}{15}$, corresponding to the first-order smoothing approximation. The curve $\Gamma(R)$ is tangent to this line at the origin, confirming the result that at low Reynolds numbers, the DIA reproduces first-order smoothing.

A couple of remarks may be made about extensions of the theory beyond the case of long-wave linear perturbations. The analysis of Sec. II does not actually depend on the precise character of $\langle \cdot \rangle$ as the projection onto functions with support in a neighborhood of zero in wave vector space; the formalism remains applicable if $\langle \cdot \rangle$ denotes the projection onto functions with support in a neighborhood of any desired wave vector. We can therefore use first-order smoothing or the DIA to investigate the behavior of a perturbation of arbitrary wave vector, although it becomes very difficult to evaluate the sums in (3.6) once k and ω become order one. When k becomes much larger than unity, corresponding to a very small-scale perturbation, the calculations again become simple. As expected, such high-wave-vector perturbations are rap-

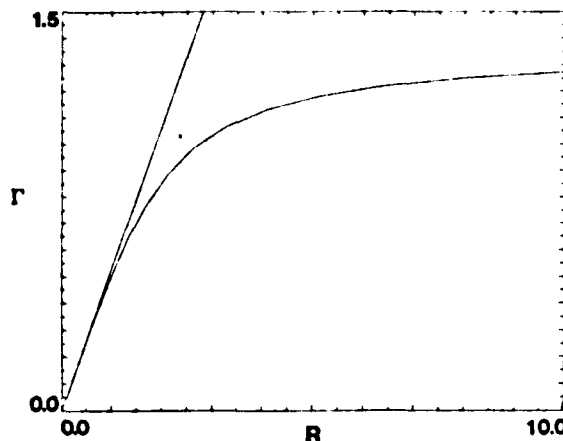


FIG. 10. Eddy viscosity factor Γ as a function of Reynolds number R .

idly dissipated by molecular viscosity, before the effect of basic flow can be felt.

We can also consider the effects of weak nonlinearity, for a perturbation of small but finite magnitude. By retaining terms of second order in the perturbation amplitude in the analysis, a quadratically nonlinear equation of motion may be obtained. The coefficient of the quadratic term can be expressed in terms of nontrivially connected diagrams, and it appears that even at this order the algebra would be too complicated to yield any information about the nonlinear dynamics. Whatever the form of the coefficient, however, it must be such as to maintain the Galilean invariance of the whole problem; that is, if a uniform translation $V_i \delta(\mathbf{k}) \delta(\omega)$ is added to the long-wave velocity $v_i^<(\mathbf{k}, \omega)$, the frequency ω must change to $\omega - \mathbf{k} \cdot \mathbf{V}$. This requirement alone is sufficient to determine that the quadratically nonlinear term has exactly the same form as the advective term in the basic Navier-Stokes equations; all the complicated corrections must cancel. Therefore, weakly nonlinear, large-scale perturbations to almost-isotropic Beltrami flow satisfy

$$\partial_t v^< + v^< \cdot \nabla v^< \approx - \nabla p^< + v_{\text{eff}} \nabla^2 v^<, \quad (5.5)$$

$$v_{\text{eff}} = v + (U_{\text{rms}} L) \Gamma(R).$$

VI. DISCUSSION

We have considered the long-wave stability properties of two viscous Beltrami flow fields, which were chosen to exhibit the features of extreme isotropy versus anisotropy. To simplify the analysis, we assumed that the flows were maintained by external body forces. Although such forced flows rarely occur in the real world, this hypothesis makes it possible to construct the stability theory in an uncomplicated manner. If it were desired, our analysis could then be extended, using multiple-scale techniques, to treat more realistic problems, such as the development of large-scale structures in slowly decaying viscous flows.

For the simple Beltrami flow, the first-order smoothing approximation correctly describes the behavior of long-wave perturbations, and instability is predicted if the Reynolds number of the flow exceeds $\sqrt{2}$. For the class of almost-isotropic Beltrami flows, both the first-order

smoothing and direct-interaction approximations indicate that the reaction of the basic flow enhances the damping of long-wave disturbances. At large Reynolds numbers, the DIA predicts that the damping rate should be essentially independent of the molecular viscosity, which agrees with an intuitive picture of the dynamics. Our results appear to be in some conflict with the general conclusions of Moffatt⁵ and Moisseyev *et al.*,⁶ and it is important to discover whether this conflict is real or whether it vanishes upon closer inspection of the particular problems analyzed. It turns out that our results are completely consistent with those of Moisseyev *et al.*⁶ for highly compressible flow, the essential difference being the degree of compressibility involved; we illustrate this by repeating the first-order smoothing calculation for almost-isotropic compressible Beltrami flow in the Appendix.

Moffatt analyzes the Arnol'd-Beltrami-Childress (ABC) flow, which is a Beltrami flow in the class (1.1) with the explicit form

$$\bar{u} = B \sin(y) + C \cos(z),$$

$$\bar{v} = C \sin(z) + A \cos(x),$$

$$\bar{w} = A \sin(x) + B \cos(y),$$

where A, B, C are real numbers. A, B, C are often chosen to be equal to unity in studies of ABC flows;⁹ this choice yields a flow which is intermediate in isotropy between our simple flow and almost-isotropic flows. An indication of the *inviscid* stability or instability of the flow may be obtained by calculating Arnol'd's second variation of the kinetic energy with respect to isocirculational displacements of the fluid particles. This functional is of indefinite sign for suitably aligned long-wave perturbations with the same helicity as the basic flow, and indeed such perturbations grow with time in the initial stages of their development.⁵ Moffatt's analytical results are supported by a recent numerical investigation of the stability of ABC flow in a viscous fluid at moderate Reynolds number.¹⁰

Despite its apparent isotropy, the ABC flow has important properties that distinguish it from the typical almost-isotropic flows investigated here. The indefiniteness of the Arnol'd functional, for example, is a property of the special orientation of the basic flow wave vectors which ceases to hold when there are more than three independent Fourier components in the flow. There are also indications that the form of Moffatt's equation of motion for long-wave perturbations, which involves the third-order differential operator $\nabla \times \nabla^2$ (hence the sensitivity to the helicity of the disturbance) gives way to a reflection-invariant form involving only a second-order operator for flows with more than three independent Fourier components. The difference between the stability properties of the ABC flow and the almost-isotropic flows may be a consequence of the difference between their topological structures. Recent investigations of the streamline structure of the ABC flow⁹ show that large regions of space are occupied by streamlines with highly regular structure, while in Beltrami flows with icosahedral symmetry, for example, or more complex cubic symmetry, it appears that almost all streamlines are ergodic.¹¹ It seems likely

that the ABC flow has more in common with our anisotropic flow than our almost-isotropic flows, as far as its stability properties are concerned.

Although the DIA gives physically sensible results for this and other problems,^{2,3} it is still an approximation. In fact, it is not even a rational approximation, in the sense that there are no indications that the omitted terms are any smaller than those retained. The most we can hope when using this technique is that it incorporate the most important physical processes sufficiently completely to give answers that are qualitatively correct. In this problem, the most important feature is probably the ability of the basic flow to mediate the transport of perturbation energy from large scales to small scales. In addition, the equations have the property that the nonlinear terms conserve the energy and helicity in the flow.

We can actually construct a model system with these essential ingredients. Imagine a large number of realizations of almost-isotropic flows, all chosen from an ensemble with well-defined statistics. We can then ask what happens if each realization is given a perturbation and then allowed to evolve according to the linearized Navier-Stokes equations; in particular, we want to know what happens to the perturbation averaged over all realizations. This situation is exactly analogous to that of the random harmonic oscillator extensively analyzed by Kraichnan.¹²

Now, consider the effect of formally coupling the dynamics of the different realizations together. The behavior will be altered, of course, with the details depending on the nature of the coupling. If the couplings are suitably restricted, however, the total energy and helicity of all the realizations taken together will still be constants of motion. The system obtained by choosing the couplings to be as random as possible within these restrictions is called the random-coupling model, and its statistical behavior is given exactly by the DIA.¹² These properties of the random-coupling model indicate that there are grounds for expecting the DIA to include at least some of the important physical effects in other systems also. Indeed, for passive-scalar dispersal in reflectionally invariant turbulence the DIA and modifications thereof have been highly successful in predicting the asymptotic long-time diffusion rate.^{2,4,13}

Unfortunately, the DIA does not always perform so successfully, particularly in the presence of helical effects. The predictions of passive-scalar dispersal in helical turbulence are in error by a factor of three,³ and helicity fluctuations in conducting fluids give rise to anomalous effects in the diffusion of magnetic fields that are inaccessi-

ble by the DIA.²³ There are also indications that helicity in the flow introduces effects that do not appear at an finite order in the perturbation expansion.⁴ Under these cumstances, we cannot present our findings as quantitative facts, but nonetheless, we believe that this work is important step in understanding the dynamical proper of helical flows.

ACKNOWLEDGMENTS

While this work was in progress, we benefited greatly from the comments and criticisms of S. A. Orszag, who also provided the facilities for performing the numerical work. We are grateful to H. K. Moffatt for sending us a copy of his work on a closely related subject, prior to publication, and for his comments on a draft of this paper. The work was supported by the U. S. Office of Naval Research under Contract No. N00014-85-K-0201 and by the U. S. Air Force Office of Scientific Research under Contract No. F49620-85-C0026. B. J. B. also thanks the National Science Foundation for financial support.

APPENDIX: INSTABILITY IN ISOTROPIC COMPRESSIBLE FLOW

Beltrami flows, in particular the family (1.1), are exact solutions of the Euler equations in an isentropic compressible fluid, and can be maintained by a suitable external agency in a viscous compressible fluid. In order to investigate the effects of compressibility on the possible generation of large-scale motions, it is simplest at first to ignore the influence of pressure forces on the dynamics of the short-wave part of the perturbation. This approximation is crucial to the analysis of Moisseyev *et al.*,⁶ who nonetheless retain the pressure in the long-wave component. For consistency, we shall neglect the perturbation pressure in all its manifestations and obtain essentially the same results.

If we neglect the perturbation pressure field (and drop the incompressibility condition, of course), the analysis of long-wave disturbances proceeds exactly as in Sec. II. The only difference is that the tensor through which two velocity components interact no longer depends only on their sum, but on their individual wave numbers

$$P'_{abc}(k^1, k^2) = k_c^1 \delta_{ab} + k_b^2 \delta_{ac} \quad (A1)$$

This tensor is no longer symmetric in *b,c*, which is the crucial feature allowing the long-wave instability. Using the first-order smoothing approximation we obtain the following equation, which is analogous to (3.3), for the evolution of a long-wave perturbation:

$$v_a^<(\mathbf{k}, \omega) = -R^2 G^0(\mathbf{k}, \omega) v_a^<(\mathbf{k}, \omega) \sum_{\hat{\mathbf{Q}} \in \mathcal{W}} [|A(\hat{\mathbf{Q}})|^2 P'_{abc}(\hat{\mathbf{Q}}, \mathbf{k} - \hat{\mathbf{Q}}) G^0(\mathbf{k} - \hat{\mathbf{Q}}, \omega) (\delta_{bd} - \hat{Q}_b \hat{Q}_d - i \epsilon_{bcd} \hat{Q}_x) P'_{cde}(-\hat{\mathbf{Q}}, \mathbf{k})] . \quad (A2)$$

For an almost-isotropic flow, evaluating the right-hand side in the long-wave limit gives

$$v_a^<(\mathbf{k}, \omega) = \frac{2}{3} R^2 G^0(\mathbf{k}, \omega) \epsilon_{abc} i k_b v_c^<(\mathbf{k}, \omega) + O(k^2) ,$$

or, in the space-time domain,

$$\partial_t v^< = \frac{2}{3} R^2 \nabla \times v^< + O(\nabla^2) , \quad (A3)$$

which predicts instabilities in the form of large-scale helical flows with helicity in the same sense as the basic flow.^{5,6}

¹G. Sivashinsky and Y. Yakhot, *Phys. Fluids* **28**, 1040 (1985).
²R. H. Kraichnan, *J. Fluid Mech.* **75**, 657 (1976); **77**, 753 (1976).
³R. H. Kraichnan, *J. Fluid Mech.* **81**, 385 (1977).
⁴I. T. Drummond, S. Duane, and R. R. Horgan, *J. Fluid Mech.* **138**, 75 (1984).
⁵H. K. Moffatt, *J. Fluid Mech.* (to be published).
⁶S. S. Moishev, R. Z. Sagdeev, A. V. Tur, G. A. Khomenko, and V. V. Yanovskii, *Zh. Eksp. Teor. Fiz.* **85**, 1979 (1983) [Sov. Phys.—*JETP* **58**, 1149 (1983)].
⁷R. B. Pelz, V. Yakhot, S. A. Orszag, L. Shtilman, and E. Le-
vich, *Phys. Rev. Lett.* **54**, 2505 (1985).
⁸H. K. Moffatt, *J. Fluid Mech.* **159**, 359 (1985).
⁹T. Dombre, U. Frisch, J. M. Greene, M. Hénon, A. Mehr, and A. M. Soward, *J. Fluid Mech.* (to be published).
¹⁰D. Galloway and U. Frisch (unpublished).
¹¹B. J. Bayly (unpublished).
¹²R. H. Kraichnan, *J. Math. Phys.* **2**, 124 (1960).
¹³R. Phythian and W. C. Curtis, *J. Fluid Mech.* **89**, 241 (1978).

END

11-87

DTIC